



FACULTY OF ENGINEERING AND SUSTAINABLE DEVELOPMENT  
Department of Electrical Engineering, Mathematics and Science

---

Development of Advanced X-ray Micro-Tomography Helical Scan and  
Tomographic Data Processing

Yoseph Abraham

Supervisor: Tunhe Zhou  
Reza Rezasson  
Examiner: Håkan Hugosson

September 2023

Student Thesis, Advanced level (Masters Degree, Two years), 30 HP  
Electronics  
Master Programme in Electronics/Automation

# Acknowledgment

I'd like to express my heartfelt thanks to everyone who contributed to this thesis. It's a result of collective efforts, and I'm truly grateful for your support. Special thanks to Tunhe Zhou, my primary supervisor, for her continuous guidance and unwavering support. I'm also thankful to Reza Rezasson my academic advisor, for his positive influence and support.

Lastly, my family's support has been invaluable and to all who played a role in my journey, thank you.

# Abstract

Micro-computed tomography (Micro-CT) is an imaging technique that allows for high-resolution, three-dimensional (3D) internal visualization of small objects in a non-destructive manner. However, a significant limitation arises when attempting to image elongated samples at higher resolutions and magnifications due to the inherently small field of view (FOV). This thesis project introduces an approach aimed at overcoming this limitation by combining helical scanning with the utilization of the open-source Astra Toolbox. The toolbox provides flexible scanning geometry parametrization and facilitates tomographic reconstruction using the Feldkamp-Davis-Kress (FDK) algorithm.

Helical data scanning represents a departure from traditional data acquisitions. Instead of capturing data at a fixed height, helical scanning acquires data by rotating and translating the imaged sample. This acquisition process extends the effective FOV, enabling the reconstruction of larger samples. To illustrate this approach, a micro-CT helical scan was performed on a pencil as an elongated sample and compared with a conventional circular scan.

While Micro-CT is a powerful imaging tool, it faces challenges when imaging weakly attenuating materials with hard X-rays. X-ray radiation possesses both amplitude and phase components, but conventional CT can only capture intensity information. This limitation often leads to poor contrast in images of weakly absorbing samples. To address this issue, the project also designed post-processing software to enhance CT image quality through phase retrieval. Phase information provides better contrast for small structures of weakly absorbing materials compared to intensity alone. The Paganin phase-retrieval algorithm is employed to retrieve this phase information, resulting in improved contrast-to-noise ratio (CNR) in tomographic reconstructions and subsequent segmentation. As a result, the generated images exhibit sharper delineations and offer a more comprehensive representation of the sample's internal structure, especially after 3-D rendering.

In summary, in this thesis, I designed the micro-CT procedure both from acquisition with an advanced helical scanning technique and from a post-processing point of view through designing software with a phase retrieval algorithm. The project has improved the conventional microCT in two aspects, namely the field of view and the phase contrast.

# Contents

<b>1</b>	<b>Introduction</b>	<b>1</b>
<b>2</b>	<b>Theory</b>	<b>2</b>
2.1	X-rays . . . . .	2
2.1.1	X-ray Sources . . . . .	4
2.1.2	X-ray Detectors . . . . .	5
2.2	X-ray Image Formation . . . . .	5
2.2.1	Absorption Contrast Imaging . . . . .	6
2.2.2	Propagation-based Phase Contrast Imaging . . . . .	6
2.2.3	Phase Retrieval . . . . .	7
2.3	Computed Tomography (CT) . . . . .	10
2.3.1	Tomographic Reconstruction . . . . .	10
2.3.2	Radon Transform . . . . .	11
2.3.3	Fourier Slice Theorem . . . . .	13
2.3.4	Filtered Back Projection (FBP) . . . . .	14
2.3.5	Feldkamp-Davis-Kress (FDK) Reconstruction . . . . .	16
2.4	Image Quality . . . . .	18
<b>3</b>	<b>Methods</b>	<b>20</b>
3.1	X-ray Micro-CT Laboratory Setup . . . . .	20
3.2	Helical Data Acquisition and Pre-Processing . . . . .	22
3.3	Phase Retrieval Method for Contrast Enhancement . . . . .	31
<b>4</b>	<b>Results and Discussion</b>	<b>35</b>
4.1	Helical Scan Reconstruction and Comparison with Conventional Scan . . . . .	35
4.2	Phase Retrieval Result and Analysis . . . . .	37
<b>5</b>	<b>Conclusion and Future Work</b>	<b>43</b>
<b>A</b>	<b>Additional figures</b>	<b>44</b>
<b>B</b>	<b>Snippet of Python Code for Paganin Phase Retrieval</b>	<b>45</b>
<b>C</b>	<b>Helical Scan Data Acquisition API with Python</b>	<b>48</b>
<b>D</b>	<b>Helical Scan Geometry Parametrization and Tomographic Reconstruction in AS-TRA using Python</b>	<b>50</b>



# List of Figures

2.1	Electro-magnetic radiation spectrum. X-rays lie in the range 0.01 nm - 10 nm . . . .	2
2.2	Phase and amplitude change when X-ray waves pass through an arbitrary medium .	3
2.3	X-ray spectrum of a tungsten tube. Bremsstrahlung emission is indicated by the continuous part of the spectrum, whereas the peaks indicate the characteristic emission [9] . . . . .	4
2.4	A basic diagram of the primary components within a micro-focus X-ray tube. Electrons are generated by applying a high negative voltage to a heating cathode. These electrons then accelerate toward a positive metal anode. En route to the target, the electron beam is magnetically focused on a smaller region, leading to the production of X-rays. However, due to their divergence, only a limited portion of the X-rays can pass through the beam spot. . . . .	4
2.5	Optically coupled indirect X-ray detection simplified diagram. The scintillator converts incoming X-rays into visible light, and the optical lenses focus the light onto a CCD detector which converts it into a digital signal [11] . . . . .	5
2.6	Absorption-based image and its corresponding profile plot. . . . .	6
2.7	In-line phase contrast and absorption imaging with a point source. . . . .	7
2.8	Phase-retrieval and tomographic reconstruction generic algorithm flow . . . . .	8
2.9	Homogeneous object with attenuation coefficient $\mu$ , incident photon $I_o$ , and attenuated intensity $I$ . . . . .	10
2.10	Non-homogeneous objects with different attenuation coefficient values . . . . .	11
2.11	Poly-chromatic radiation with non-homogeneous object . . . . .	11
2.12	Coordinates of Radon transform . . . . .	12
2.13	Ideal parallel beam . . . . .	12
2.14	Fourier slice theorem . . . . .	13
2.15	Fourier transform-based reconstruction flow . . . . .	14
2.16	Single-intensity image back projection hardly gives an estimate of the original function $f(x, y)$ . . . . .	14
2.17	Frequency domain sampling/polar sampling . . . . .	15
2.18	Commonly used ramp filters during filtered back projection reconstruction . . . . .	16
2.19	Commonly used geometric setups for X-ray CT scanning . . . . .	16
2.20	Coordinate system for FDK algorithm for a circular cone-beam geometry. A point of the reconstructed object is taken along its xyz coordinates, while the detector registers the data on the specified pixel coordinates( $x', z'$ ). An instance of rotation is shown where the source and detector have rotated at an angle of $\beta$ . . . . .	18
2.21	Illustration of resolution, contrast, and noise . . . . .	18
3.1	Directions when the sample theta stage is at 0 degrees: The z and x axes rotate with the sample stage. When the sample theta stage is set to -90 degrees, the z-axis moves perpendicular to the beamline, while the x-axis moves parallel to the beamline . . .	21
3.2	Mounting of the scanned sample on the micro-CT scanner for helical data acquisition. The red arrow indicates the pencil and the green arrow indicates the sample holder for mechanical stability. . . . .	22
3.3	Example of collected projection images taken with their respective intensity profile plot and dynamic range. The flow shows the flat-field correction stage from the first row to the last. Intensity profile plots are taken from the yellow box region. . . . .	24

3.4	The projection image is prepared for reconstruction, by taking the negative logarithm of the flat-field corrected image and its corresponding profile plot. . . . .	25
3.5	The overall flow of the helical scanning technique. . . . .	26
3.6	Demonstration of the sample outside of FOV . . . . .	26
3.7	One projection image of a pencil where the entire vertical FOV is fitted. . . . .	27
3.8	Parametrization of cone-beam geometry scanning in ASTRA Toolbox. . . . .	27
3.9	Helical scan modeling according to the ASTRA toolbox cone-beam geometric parametrization. . . . .	28
3.10	Illustration of how FOV is affected by the X-ray source and detector distance placement from the scanned sample. . . . .	29
3.11	Conventional scan projection image for reconstruction and its corresponding profile plot for the entire projection. The dynamic intensity range is $[0, 1]$ . . . . .	30
3.12	Volume geometry convention in Astratool box. Voxel sizes are set with equal dimensions on all sides. . . . .	30
3.13	ASTRA toolbox programming interface architecture and reconstruction concept. . .	31
3.14	Scanned insect (dung-beetle) at SUBIC with the micro-CT scanner. The red arrow indicates where the area of the scan was made. . . . .	32
3.15	Projection image before after flat-field correction and corresponding histogram. . . .	33
3.16	The procedure followed for phase retrieval, from data handling to parameter selection. 34	
4.1	Reconstructed slice for both helical and conventional scans. . . . .	35
4.2	Artifacts in the helical scan from a top view and side view. . . . .	37
4.3	A user interface for Paganin phase retrieval. Corresponding parameter values are inserted manually, and the filtering process is done interactively. . . . .	38
4.4	Projection image of 3.15b and its histogram after phase retrieval. . . . .	38
4.5	Reconstructed slice of dung beetle before and after phase-retrieval. . . . .	39
4.6	Reconstructed slice before and after phase-retrieval black arrow indicates the ROI and its corresponding statistical values, while the yellow arrow indicates the background. 40	
4.7	Corresponding histograms for the entire slice in Fig. 4.6. . . . .	40
4.8	Segmentation of ROI using thresholding method before and after phase retrieval. The orange coloring is the background and black is the ROI. . . . .	41
4.9	3-D rendered image of the scanned sample before and after phase-retrieval . . . . .	42
A.1	3-D rendered image of the scanned sample upper and lower left eye part. . . . .	44

# Chapter 1

## Introduction

X-ray computed tomography (XCT) is a non-destructive inspection technique initially designed for medical imaging but is now widely adopted in industrial applications. Its fundamental principle involves reconstructing a cross-sectional image of an object using a finite set of two-dimensional images and digital radiographic projections taken from various angles. The cross-sectional image of the object can be rendered in 3D, and its internal structure can be reconstructed and analyzed without the need for physical dissection. This technique is used for non-destructive quality inspection and dimensional analysis of materials. A typical application of CT with X-ray radiation is the detection of flaws, cracks, and particle analysis in materials, as well as electronic circuit board weld quality inspection [1] and inspecting production lines, such as in automotive production [2]. It is also employed for inspecting body parts in automotive manufacturing. A geometric setup and movement system facilitate the relative motion between the CT system, which comprises the X-ray source and X-ray detector, and the object being examined. Different scanning methods are available depending on the flexibility of the manipulation system, with 3D cone-beam CT being the most prominent and extensively used.

It is known that electromagnetic radiation has both amplitude and phase. However, when we observe an image, we can only extract intensity information (amplitude), meaning that we don't have direct access to the phase information. Sometimes the detected intensity through absorption contrast results in poor contrast for weakly attenuating materials, leading to images with poor contrast that can be challenging to interpret. Part of the project's objective is to implement user-friendly software for processing micro-CT images, starting with basic flat-field correction where the tomographic images are adjusted for non-uniformities and artifacts in X-ray images. The goal is also to retrieve phase information to produce a reconstructed image suitable for segmentation and 3-D rendering. The Paganin method proposed by [3] has been implemented as a phase-retrieval algorithm.

Additionally, the project aims to implement a helical scanning method and tomographic reconstruction in a micro-CT X-ray lab by controlling the rotational and translational movement of the sample to position it within the field of view (FOV) during tomography acquisition. The geometric specification is then parameterized for each projection image using an open-source tomographic processing toolbox, namely the Astra toolbox developed by [4], for reconstructing the tomographic data. This enables the scanning and processing. For reconstruction, the FDK (Feldkamp, Davis, and Kress) reconstruction algorithm has been used, which is frequently applied in cone-beam tomography [5].

The thesis is organized into several chapters. Chapter 2 covers the theoretical background of X-rays, X-ray image formation, processing, and tomographic reconstruction. Chapter 3 discusses the laboratory setup, the method used to acquire a helical tomographic scan, and its reconstruction, followed by the utilization of Paganin phase retrieval for contrast enhancement and development. Chapter 4 presents the results and analysis of the helical scan in comparison to the conventional scan, as well as Phase retrieval on an actual scanned sample. Chapter 5 concludes the work with relevant conclusions and outlines future prospects for the project.

# Chapter 2

## Theory

In this chapter, the underlying science behind X-rays' interaction with matter, X-ray image formation, and processing i.e. phase retrieval, and tomographic reconstruction algorithms are discussed, while the relevant methods used are also motivated.

### 2.1 X-rays

The interaction of X-rays with matters is the basis for understanding X-ray imaging. X-rays are electromagnetic radiation similar to visible light but have much shorter wavelengths (and higher photon energies) as shown in Fig. 2.1.

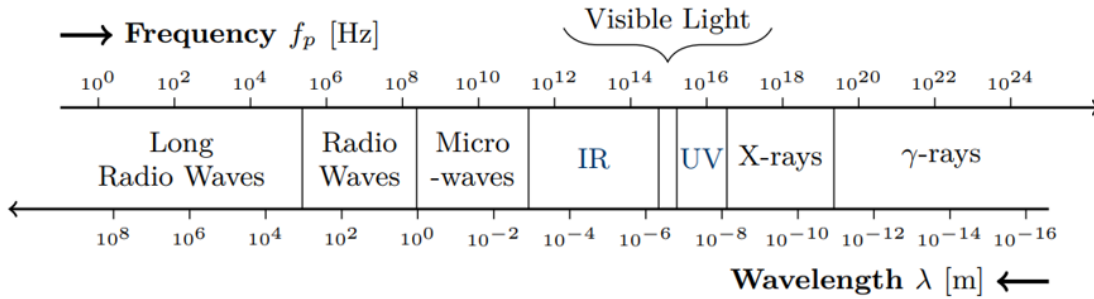


Figure 2.1: Electro-magnetic radiation spectrum. X-rays lie in the range 0.01 nm - 10 nm [6]

Both the photon energy and wavelength are used to describe the electromagnetic radiation in the X-ray region. The equation below relates the wavelength  $\lambda$  and photon energy  $E$ .

$$E = \frac{ch}{\lambda}, \quad (2.1)$$

where  $c=299,792,458$  m/s is the speed of light,  $h=6.626 \times 10^{-34}$  J s is Planck's constant, and energy is given in Joules. It is commonly written as;

$$E[keV] \approx \frac{1.239}{\lambda[nm]}, \quad (2.2)$$

Compared to visible lights, X-rays possess higher energy, which results in two significant differences: they can easily pass through thick/opaque objects (due to lower interaction with matter) and strong ionization (releasing electrons from atoms and producing ions resulting in secondary interaction).

A plane wave of electromagnetic radiation traversing in an empty space (vacuum), in the  $z$ -direction is described by the equation below

$$U = U_0 e^{ikz}, \quad (2.3)$$

where  $k = \frac{2\pi}{\lambda}$  is the wavelength number (wave number),  $\lambda$  is the wavelength,  $U_o$  is the incoming wave amplitude, and  $U$  is wave amplitude after through the medium. This expression is only valid in vacuum space. In optics, the refractive index is a dimensionless ratio between the speed of light  $c$  in a vacuum, and  $v$ , the speed of light inside a material:

$$n = \frac{c}{v}, \quad (2.4)$$

Equation (2.5) describes the refraction of light as it travels from one medium to another (for example from air to water). A refractive index value of 1 corresponds to a vacuum. Since X-rays have higher energy than visible light, they penetrate through objects easily. Material's refractive index value  $n$  is close to 1 under X-rays and can be described by the equation below.

$$n = 1 - \delta + i\beta, \quad (2.5)$$

where  $\delta$  is proportional to the phase shift and complex part  $\beta$  is proportional to the amplitude change. The real part of the refractive index can be expressed as:

$$\delta = \frac{2\pi p_a Z r_o}{k^2}, \quad (2.6)$$

where  $p_a$  is the atomic number density,  $Z$  is the atomic number,  $r_o$  is the classical electron radius and  $k$  is the magnitude wave vector. And the imaginary part  $\beta$  can be expressed as

$$\beta = \frac{p_a \sigma_a}{2k}, \quad (2.7)$$

where  $\sigma_a$  is the absorption cross-section.

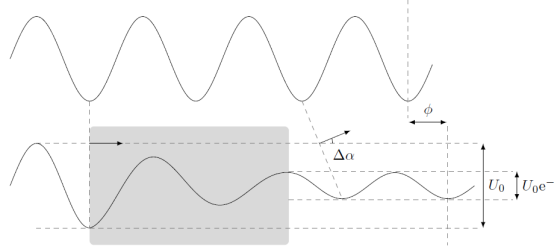


Figure 2.2: Phase and amplitude change when X-ray waves pass through an arbitrary medium

Fig. 2.2 shows when a wave propagates through a medium with a refractive index of  $n$ , how wave amplitude  $U_o$  decreases by  $e^{-a}$  and phase is shifted by  $\phi$ . Equation (2.3) can be expanded as follows

$$U(z) = U_o e^{iknz} = U_o e^{ikz} e^{-ik\delta z} e^{-k\beta z}, \quad (2.8)$$

The first part indicates an un-interfered wave with a unity refractive index, which is the impacting wave. The next two exponential parameters  $\delta$  and  $\beta$  change the wave property. The first exponential describes the phase shift, compared to the original wave being phase shifted by  $-k\delta z$ , labeled as  $\phi$ . In the  $x, y, z$  space, it can be described as:

$$\phi(x, y) = -\frac{2\pi}{\lambda} \int \delta(x, y, z) dz, \quad (2.9)$$

The second exponential function accounts for the absorption factor. The change in the intensity is given by the square of the amplitude change  $(e^{-k\beta z})^2 = e^{-2k\beta z}$ . The factor  $2k\beta = \frac{4\pi}{\lambda}\beta$  is the attenuation coefficient;

$$\mu = \frac{4\pi}{\lambda}\beta, \quad (2.10)$$

### 2.1.1 X-ray Sources

There are multiple types of X-ray sources. The common laboratory X-ray tubes generate X-rays by hitting a metal target with high-power electrons. Such dense electrons are generated by applying high potential difference, i.e. negative voltage applied to a cathode material (commonly filament is used). This leads to the filament giving off high energy and accelerated electrons [7]. The externally applied high voltage accelerates the electrons. When this beam of electrons reaches the anode material (e.g. tungsten, or other materials). Two kinds of X-rays are produced. One is known as Bremsstrahlung when the electron passes close to the atomic nucleus, where deceleration in the electric field causes the electrons to lose kinetic energy to be converted to photons [8]. The second is characteristics line emission, where an incident electron ionizes an off-the-target material (when an electron in the target atom falls down to a lower energy state to fill in the vacancy due to ionization). Once this hole is created due to ionization, another electron comes in to fill the empty spot and produces a photon to remove its surplus energy. This photon gives X-rays of specific energy levels (discrete ones) which depend on the chemical elements of the target material. The figure below shows the X-ray spectrum for a tungsten tube based source.

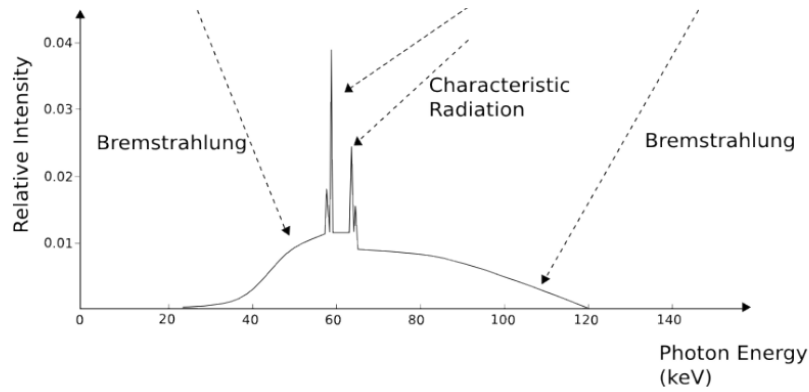


Figure 2.3: X-ray spectrum of a tungsten tube. Bremsstrahlung emission is indicated by the continuous part of the spectrum, whereas the peaks indicate the characteristic emission [9]

X-ray sources can be as big as synchrotron facilities where photon density is higher, or relatively smaller ones as what is commonly found in health or industrial facilities. This section describes an overview of the operating principles behind X-ray generation and detection. During the work of the thesis, the X-ray source used was a micro-focus X-ray tube type. Figure 2.4 depicts the simplified schematic of the main components inside a micro-focus X-ray tube.

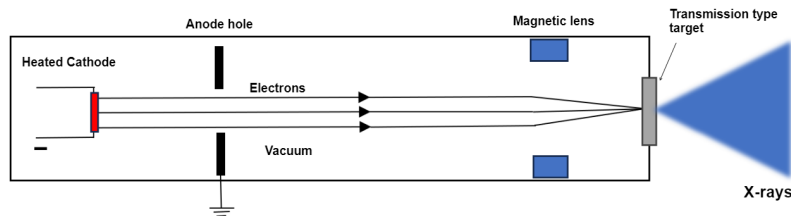


Figure 2.4: A basic diagram of the primary components within a micro-focus X-ray tube. Electrons are generated by applying a high negative voltage to a heating cathode. These electrons then accelerate toward a positive metal anode. En route to the target, the electron beam is magnetically focused on a smaller region, leading to the production of X-rays. However, due to their divergence, only a limited portion of the X-rays can pass through the beam spot.

### 2.1.2 X-ray Detectors

X-rays that are generated from the source need to be properly detected by electronic sensing devices so that the data captured can be processed digitally. Traditionally, the generated X-ray images in medical imaging or industrial applications were detected on a film after traversing a certain distance [10]. Nowadays, the acquired X-ray images need to be stored and displayed digitally. Flat panel detectors are among the common types of detectors, as the name implies where a flat and matrix-like arrangement of photo-diode sensors detect incoming photons. Commonly X-rays produce electron-hole pairs inside the detector material, X-ray interaction with matter was explained in the previous sections. The sensor's job is to detect this electron-hole pair phenomenon and convert it to an electrical signal. There are two methods for detecting X-rays. One is the direct method, and the other is indirect [11]. The detector is placed behind the object of interest (the object being scanned) and records the intensity of X-rays. The X-rays exhibit a wave propagation property as they traverse through free space, and interact with the detector in the form of photons [7]. This is an indirect method of detection since incoming X-rays are converted into photons. The first step is to convert the X-ray radiation into visible light. This is done with the help of scintillators (e.g. CsI: Tl, GOS, Tb). The light is then encoded into an electrical signal by an array of detectors, for example, charge-coupled devices (CCD), which are made out of metal-oxide-semiconductor capacitors, and are light-sensitive. A larger area of detection can be covered by coupling the CCDs creating an array of detectors. Incoming luminescence converted by the scintillators can be focused onto the array of detectors using an optical lens setup, like the one used in this thesis. Such coupling does introduce a lower signal-to-noise ratio, as it reduces the number of photons hitting the CCD arrays [11]. An overview of the indirect detection method optically coupled and with a CCD detector is shown in the figure below.

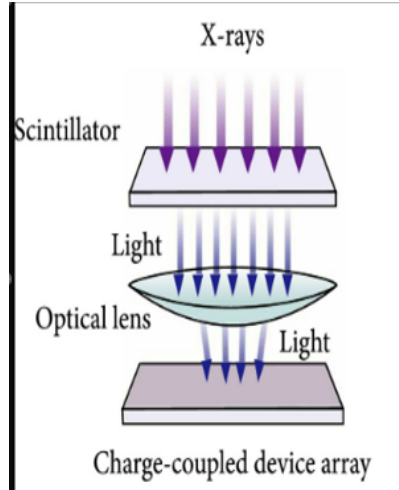


Figure 2.5: Optically coupled indirect X-ray detection simplified diagram. The scintillator converts incoming X-rays into visible light, and the optical lenses focus the light onto a CCD detector which converts it into a digital signal [11]

## 2.2 X-ray Image Formation

An X-ray image is formed by recording the varying intensity of the X-rays passing through an object of interest. X-rays interact with the material while passing through it, and the interaction can be characterized by the material's refractive index, shown in Equation (2.5). Every material has its own refractive index, depending on atomic number and chemical composition. The refractive index of the material describes how X-ray interacts with the matter. The proportionality of  $\delta$  to the phase shift and the proportionality of the complex part that includes  $\beta$  to the attenuation coefficient can be observed.

### 2.2.1 Absorption Contrast Imaging

The interesting nature of X-rays is the fact that one can image the interiors of visually opaque objects. Conventional X-ray imaging is based on the absorption properties of the sample. An object that is being imaged by X-rays has its own refractive index value based on its chemical composition, but for most materials, it is hard to find the exact number as they are composites of different materials. The traditional way of X-ray imaging, passes the waves through the object with a detector lying behind it, by recording the attenuation in the intensity. Different parts of the object with different densities will attenuate X-rays differently, hence forming the image on the detector.

Figure 2.6a shows an attenuation-based image of an Arduino nano circuit board that was scanned at SUBIC (Stockholm University Brain Imaging Center) and its corresponding grayscale values indicating the intensity level shown in Fig. 2.6b. The detector is a scintillator-coupled CCD camera. Therefore, the intensity value is not the real photon count. The projection is a 16-bit image with a maximum intensity value of 65535.

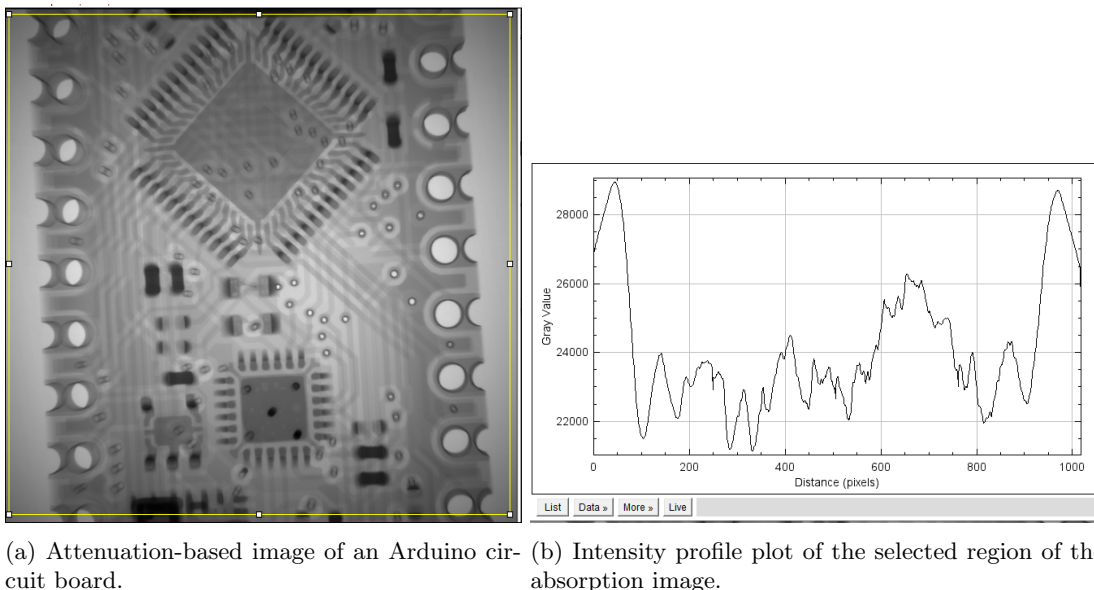


Figure 2.6: Absorption-based image and its corresponding profile plot.

### 2.2.2 Propagation-based Phase Contrast Imaging

X-ray detectors record the intensity of incoming X-rays after passing through an object of interest. The frequency of X-rays is too high to be measured directly, so the phase shift needs to be converted to intensity variations at the detector [7]. Sometimes the phase of a signal carries relevant information in characterizing the imaged object with a better contrast compared to absorption-based imaging. By using the transport of intensity equation, which shows the intensity variation of X-rays, it is possible to extract phase information leading to higher contrast and details of the imaged object (higher signal-to-noise ratio and better image quality).

The phase of a periodic signal (or electromagnetic wave) is a real-valued scalar that describes the relative location of each point on the wavefront within the span of each period [12], typically expressed in radians. The amplitude component of X-rays is easier to understand as it describes the intensity and that is the only thing we can detect directly. Detectors cannot directly measure the phase information and are only sensitive to intensity variations. An object of low attenuation coefficient, such as soft tissue, shows lower intensity variation in comparison to phase contrast [13]. According to [13], a 50  $\mu\text{m}$  thick soft-tissue can barely attenuate a 17.5 keV, but the phase shift of the X-rays due to refraction is almost  $\pi$ , which makes measuring the phase information produce a better image contrast than the absorption.

The difference between conventional absorption contrast imaging and inline phase-contrast imaging is the arrangement while scanning, which is in the propagation distance of the waves. In absorption, projection is captured at a plane close to the sample, whereas in in-line phase-contrast imaging, the X-rays are made to propagate some distance through free space after leaving the sample, then



registered by the detector, if the propagation distance is chosen properly, the imaged projection will consist of edge enhancements [14]. Figure 2.7 shows the case where the detector is put as close as possible to the imaged object  $R_1$ , the image acquired from such arrangement is dominated by an absorption contrast. When the detector is placed in  $R_2$  position a phase-contrast image is developed, where the incident X-ray beam is refracted after the propagation distance of  $R_2$ . Different prop-

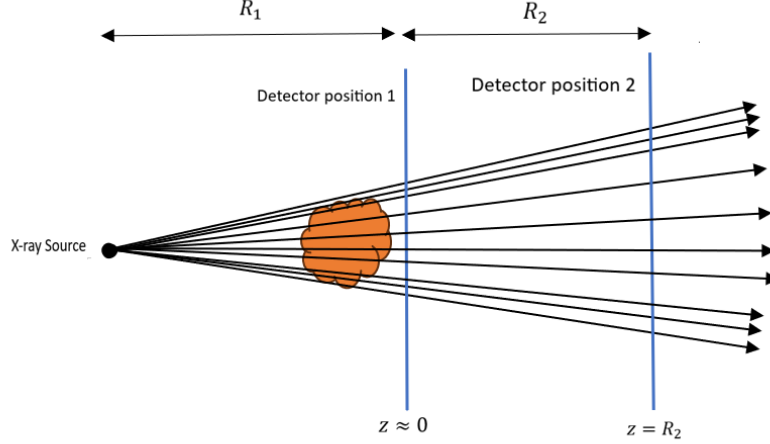


Figure 2.7: In-line phase contrast and absorption imaging with a point source.

agation distances result in different imaging techniques, when the propagation distance increases the imaging goes from absorption-contrast imaging  $\rightarrow$  near-field imaging  $\rightarrow$  far-field regime [8]. For phase contrast imaging or phase retrieval, propagation distance for near-field imaging is used. In the near-field regime, an edge enhancement effect is created due to the refracted X-ray waves after propagating  $R_2$  distance.

### 2.2.3 Phase Retrieval

In propagation-based phase contrast imaging, both absorption and phase shift of the X-rays contribute to the signal. In order to do a quantitative analysis of the images, the phase shift needs to be retrieved numerically. There are different phase retrieval algorithms, among the most commonly used is the Paganin method which has been utilized in different tomographic processing tool packages [15, 16, 17, 18]. The Paganin method is an analytical method that was introduced by [3], where it is possible for both the phase and amplitude details to be extracted from a single out-of-focus image of a homogeneous object. Phase-sensitive detection arrangements used in phase-contrast imaging do not offer enough quantitative phase data that is suitable for tomographic reconstruction. As a result, the application of phase retrieval algorithms becomes necessary to obtain the required information for the phase reconstruction process [14]. Paper [14] compares 7 phase retrieval methods that are applicable to tomography, where it is possible to retrieve the phase-shift information using only one image per projection. Generally in order to retrieve phase-shift information of an image analytically, at least two projection images are required [14], such projection images are taken at two different distances from the X-ray source, this is because only one projection image taken from a single distance, both the attenuation and phase shift signals are tangled and can't be calculated from a single registered intensity distribution [19]. So in a tomographic scanning setup, taking projection images at two different distances will complicate the phase-retrieval process and is difficult to arrange experimentally [14]. The Paganin phase retrieval method can also be considered as a low pass filter, reducing the noise and dynamic range of an X-ray image, and was utilized by [17] in their parallel-beam tomographic data processing package, which aids in improving the contrast of materials that might otherwise be difficult to distinguish. Paper [14] compared 7 different phase retrieval methods and concluded that the algorithms follow the same pattern even though their mathematical derivation is different.

The phase retrieval procedure is illustrated in Fig. 2.8. As an input, it takes:  $I(r_\perp)$ , the image plane registered as a function of transverse function  $r_\perp = (x, y)$  on the detector pixel coordinate.

Then the function  $g(I(r_\perp))$  is calculated, which depends on the type of algorithm one is using, where for the Paganin method, it is a normalization of the raw projection image  $\left(\frac{I}{I_0}\right)$ , where  $I_0$  is the flat-field image (projection image without an object in the middle of the source and detector). The function  $g(I(r_\perp))$  is then filtered in the frequency domain, so  $g(I)$  is Fourier transformed and multiplied by a filter function  $H_p(w)$ , where  $w = (u, v)$  is the spatial frequency. The filter used,  $H_p(w)$ , depends on the method used to retrieve the phase, as stated by [14]. Finally, by taking the inverse 2-D Fourier transform the function  $F^{-1}(g_F)$  of the filtered quantity, the 2D phase distribution  $\phi(r_\perp)$  can be extracted.

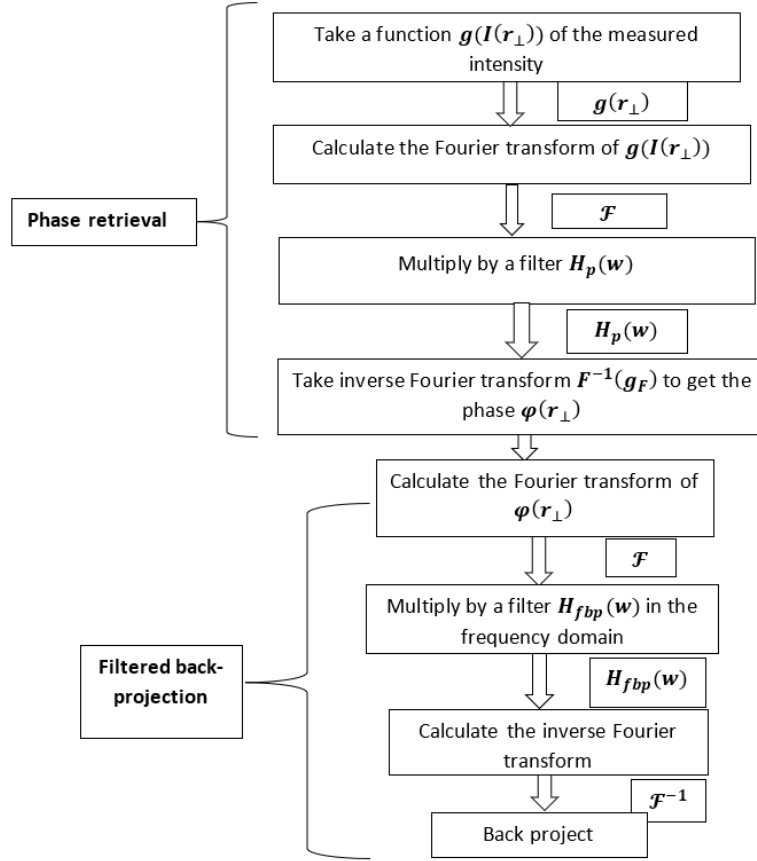


Figure 2.8: Phase-retrieval and tomographic reconstruction generic algorithm flow

If we are considering a plane wave monochromatic X-ray with unity intensity propagating along the direction of the optic axis  $z$ , transmitted X-ray intensity, and phase shift are described by Equation (2.11) and Equation (2.12) respectively.

$$I(r_\perp) = I_{\text{in}} e^{-\int \mu(r_\perp, z) dz}, \quad (2.11)$$

where  $I(r_\perp)$  is the intensity registered by the detector spatial coordinate  $r_\perp$ , and  $I_{\text{in}}$  is the incident X-ray intensity. For a homogeneous material, having a uniform absorption coefficient, the above equation can be approximated according to Beer-Lambert's and is introduced in Equation (2.18), and the phase shift is shown in Equation (2.9) and can be approximated to [14],

$$\phi_\lambda(r_\perp) = -\frac{\delta_\lambda T(r_\perp) 2\pi}{\lambda}, \quad (2.12)$$

where  $T(r_\perp)$  is the projected thickness of the homogenous material. The phase shift  $\phi$  introduced by the sample to the X-ray beams is proportional to the real part of the refractive index  $\delta$ , and the

attenuation coefficient  $\mu$  is proportional to the imaginary part of the refractive index  $\beta$  as shown in Equation (2.10).

Paper [17] makes use of the Paganin filter as a low pass filter to remove high-frequency components such as edges from projection images. They mention that for applications that only use absorption-contrast data, the edge enhancement due to propagation-based phase contrast effect for synchrotron-based tomography (parallel beams) introduces a noise (artifact) known as streak artifact after reconstructing the image. The edge-enhanced effect is important for applications focusing on material interfaces rather than their densities for example in studying crack formation in steels, rocks, or bones. However, this effect can lead to streak artifacts and significant fluctuations in grayscale values between interfaces in reconstructed images [20]. These drawbacks pose challenges for post-processing techniques, such as image segmentation or image rescaling, impacting their performance, the Paganin filter used as a low pass filter is useful in such cases. The Paganin filter was utilized by [8] to retrieve the phase map of a paperboard for a quality control test, in order to find out the material's thickness distribution. After tomographic reconstruction of the phase-shift distribution, which eventually gave them a better density distribution of the material, compared to a reconstruction without phase-retrieval.

In order to use the Paganin phase retrieval method in more practical cases, such as in a cone-beam geometrical setup, paper [14] shows how to modify the algorithm. Meaning that the source is placed at a finite distance from the object and the illumination is a spherical wave. We consider the source located  $R_1$  away from the object and the object  $R_2$  distance away from the detector as shown in Fig. 2.7. In the cone beam geometrical case, the object is magnified by a geometric magnification factor of  $M = \frac{R_1+R_2}{R_1}$ . The main derivation of the Paganin phase retrieval method is based on solving the transport of intensity equation (TIE) [3], given by;

$$\nabla_{\perp} (I(r_{\perp}, z) \nabla_{\perp} \phi_{\lambda}(r_{\perp}, z)) = -\frac{2\pi}{\lambda} \frac{\partial}{\partial z} I(r_{\perp}, z), \quad (2.13)$$

where  $\nabla_{\perp}$  is the gradient operator in the detector spatial plane  $r_{\perp}$ , and  $I(r_{\perp})$ ,  $\phi$  are the intensity and phase of the beam, respectively. The solution to this equation is finding the phase-shift  $\phi$ , and [3] have shown in their paper how to extract phase information. Different papers put the final solution in different formats since they use different X-ray imaging setups but the overall phase retrieval procedure is the same as shown in Fig. 2.8. For a cone-beam case, the final equation from Paganin et al [3] is given as:

$$\varphi(x, y) = \frac{1}{2} \frac{\delta}{\beta} \ln \left( \mathcal{F}^{-1} \left\{ \frac{\mathcal{F} \left[ \frac{I(x, y)}{I_0(x, y)} \right]}{1 + \frac{\lambda z_{\text{eff}}}{4\pi} \frac{\delta}{\beta} (u^2 + v^2)} \right\} \right), \quad (2.14)$$

where  $I(x, y)$ , is the registered intensity at the detector,  $\mathcal{F}$  and  $\mathcal{F}^{-1}$  are the Fourier transform and inverse Fourier transform respectively,  $I_0(x, y)$  is the incident X-ray intensity,  $z_{\text{eff}}$  is the effective propagation distance given by,  $\frac{R_2}{M}$ , which according to [14] is the most important factor that should be considered if the Paganin method is to be used in cone-beam setup, and  $u, v$  are the spatial frequencies given by the equations below [17].

$$u = \frac{u_i}{\Delta x} = \frac{i}{W} \cdot \frac{1}{\Delta x}; \quad i = -\frac{W}{2}, -\frac{W}{2} + 1, \dots, \frac{W}{2} - 1, \frac{W}{2}, \quad (2.15)$$

$$v = \frac{v_j}{\Delta y} = \frac{j}{H} \cdot \frac{1}{\Delta y}; \quad j = -\frac{H}{2}, -\frac{H}{2} + 1, \dots, \frac{H}{2} - 1, \frac{H}{2}, \quad (2.16)$$

where  $W$  and  $H$  are the width and height of the image in pixel number,  $\Delta x$  is the pixel size of the detector, and  $i, j$  are integer indices.

As can be seen from Equation (2.14), the approximate solution to TIE Equation (2.13) is a convolution process with a filter, and the filter term is represented by the equation below:

$$H_p = \frac{1}{1 + \frac{\lambda z_{\text{eff}}}{4\pi} \frac{\delta}{\beta} (u^2 + v^2)}. \quad (2.17)$$

The  $\frac{\delta}{\beta}$  is manually chosen for homogeneous material only and is unknown for multi-materials. The  $\frac{\delta}{\beta}$  value is mainly chosen as a trade-off between contrast enhancement and the sharpness

of a reconstructed image and can empirically be chosen between 10 to  $10^4$  according to [17]. By combining phase-retrieval algorithms with computed tomography, it becomes possible to reconstruct the detailed distribution of complex refractive index in the three-dimensional representation of the scanned object [18].

## 2.3 Computed Tomography (CT)

Sometimes there is difficulty in observing features of interest after acquiring a single X-ray image, mainly due to structural overlap since the image is taken from one direction, limiting the possibility of seeing small and faint features [19]. Computed tomography (CT) solves this problem by taking X-ray images from multiple angles usually up to 360/180 degrees, and building 3-D images of the internal structures. CT technology was a huge success in 1979 when Alan Cormack and Hounsfield were given the Nobel Prize for inventing it [21]. Although CT is commonly associated with tomography, other imaging modalities such as infrared light OCT, ultrasound, and microwave techniques can also be utilized for performing tomographic procedures [6].

### 2.3.1 Tomographic Reconstruction

The main concept behind CT is to determine the linear attenuation coefficient of the object being scanned and convert this to grayscale value [22]. The attenuation coefficient is measured in units per meter as shown in Equation (2.10).

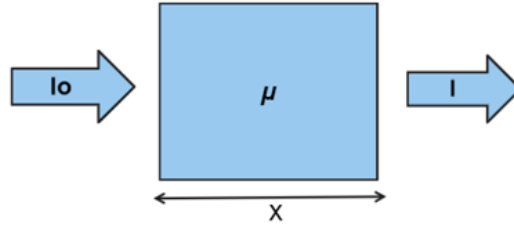


Figure 2.9: Homogeneous object with attenuation coefficient  $\mu$ , incident photon  $I_o$ , and attenuated intensity  $I$

As shown in Fig. 2.9, the incident photon intensity,  $I_o$ , when it is monochromatic (highly filtered, coherent, with discrete photon energy levels), and passes through a homogeneous object with an attenuation coefficient,  $\mu$ , Beer-Lambert law explains the incident photon's attenuation level changes according to the material's thickness,  $x$ , and attenuation coefficient  $\mu$ :

$$I = I_o \cdot e^{-\mu x}, \quad (2.18)$$

Since most of the materials being scanned don't have homogeneous attenuation coefficient distribution, as shown in Fig. 2.10, due to different material type composition, the Beer-Lambert equation can be modified to take into account such variation.

$$I = I_o \cdot e^{-(\mu_1 x_1 + \mu_2 x_2 + \mu_3 x_3 + \dots + \mu_n x_n)}, \quad (2.19)$$

$$I = I_o \cdot e^{-\sum_{i=1}^n \mu_i x_i}, \quad (2.20)$$

Most X-ray CT scanners have poly-chromatic radiation, meaning that the source produces an X-ray beam with a wide range of photon energies, unlike monochromatic radiation, as shown in Fig. 2.11 so modifying the last equation, we get;

$$I = \int_0^{E_{\max}} I_o(E) \cdot e^{-\int_0^x \mu(x') dx'} dE, \quad (2.21)$$

If we are working with a raw attenuation image, applying a negative logarithm to the ratio of the

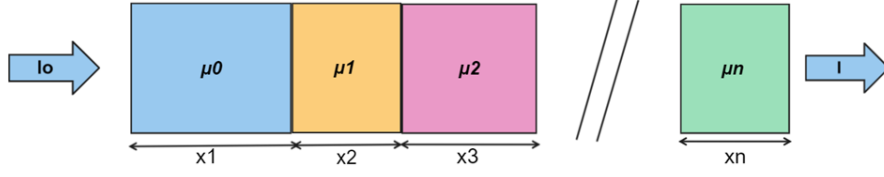


Figure 2.10: Non-homogeneous objects with different attenuation coefficient values

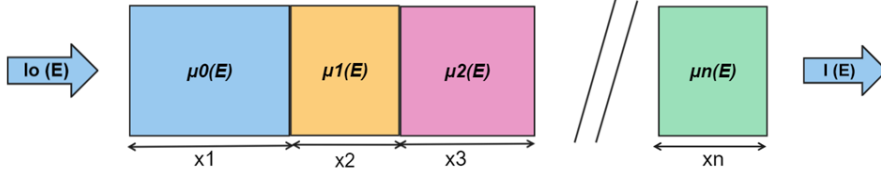


Figure 2.11: Poly-chromatic radiation with non-homogeneous object

incident photon to attenuated photon, gives what is called ray sums.

$$-\ln\left(\frac{I}{I_0}\right) = \int_0^x \mu(E)x \, dx, \quad (2.22)$$

The above equation is what we call a projection image, It is a normalized signal summing the attenuation coefficient of the object along the X-ray path. Tomographic reconstruction is used to estimate this attenuation coefficient value and can be done either analytically or iteratively through different reconstruction methods [22].

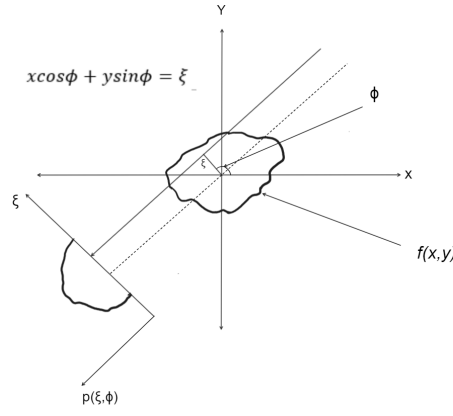
### 2.3.2 Radon Transform

To understand how Computed Tomography works, we need the mathematical description behind tomography by Radon transform, described in a paper that was published in 1917 [23]. It is used to compute the projection images of an object by capturing data from various rotation angles [19]. The Radon transform of a particular cross-section generates an image in which one dimension represents the spatial coordinate within the section's plane and is perpendicular to the direction of the radiation. The other coordinate is the rotation angle. The maths can be described below, in a 2-D space. The X-rays are assumed to be generated in a perfectly parallel manner for the sake of simplifying the explanation. The object being scanned is represented by 2-D spatial coordinate function  $f(x, y)$ , the value representing the registered grey scale value (attenuation coefficient), and the function  $f(x, y)$  should be integrable [24]

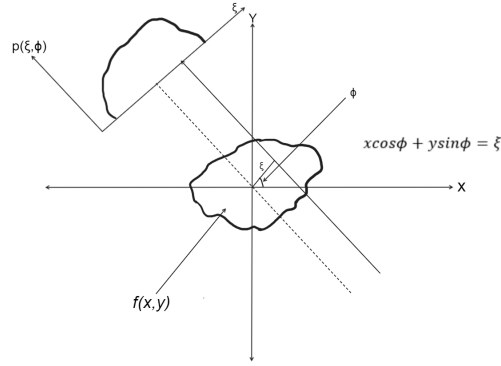
$$p(\xi, \phi) = \int_{-\infty}^{\infty} \int_{-\infty}^{\infty} f(x, y) \delta(x \cos \phi + y \sin \phi - \xi), dx, dy, \quad (2.23)$$

The term  $\delta$  is a Dirac function (impulse function) used to select lines that lie within the line equation  $x \cos \phi + y \sin \phi = \xi$ . This can be seen in Fig. 2.12.

The coordinates  $x$ ,  $y$ ,  $\xi$ , and  $\phi$  are expressed geometrically as shown in the figure below:



(a) Angular position 1



(b) Angular position 2

Figure 2.12: Coordinates of Radon transform

The Radon transform function output  $p(\xi, \phi)$  is the registered projection of the image. For the sake of simplifying the explanation, a line traversing across has been considered. The basic concept of the Radon transform is that the function  $f(x, y)$  can be uniquely represented by all the straight-line integrals over its domain [24]. In Fig. 2.13 ideal case of a perfectly parallel beam passing through an object with the function distribution  $f(x, y)$  is shown.

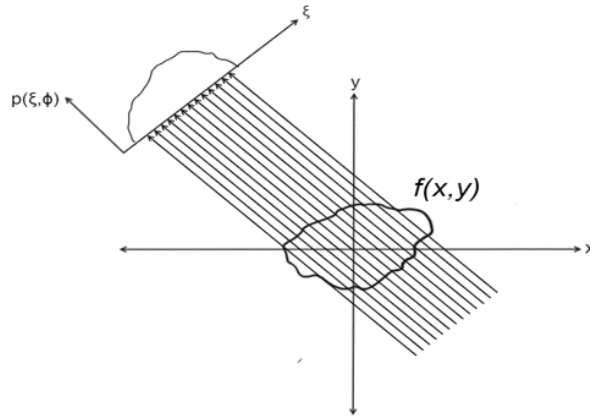


Figure 2.13: Ideal parallel beam

A complete set of tomographic images is obtained by rotating over 180 or 360 degrees, depending on the X-ray scanning geometry. For parallel beams, the rotation is usually 180 degrees, while for

cone-beam configurations, it is typically 360 degrees. The main challenge in tomography lies in reconstructing a section of the object from the sinogram or projection data. This process involves solving the inverse problem i.e. the inverse Radon transform. The goal of reconstruction, such as in CT or micro-CT, is to estimate the original function  $f(x, y)$  from the measured line integral values. This reconstruction process solves the inverse Radon transform using experimental measurements. The concept of tomographic reconstruction and the solution to the inverse Radon transform can be understood by considering the Fourier slice theorem.

### 2.3.3 Fourier Slice Theorem

Fourier slice theorem or Central slice theorem looks into the frequency domain property of the spatial image function and its tomographic (slice) image counterpart. Figure 2.14 below shows the relationship in the frequency domain.

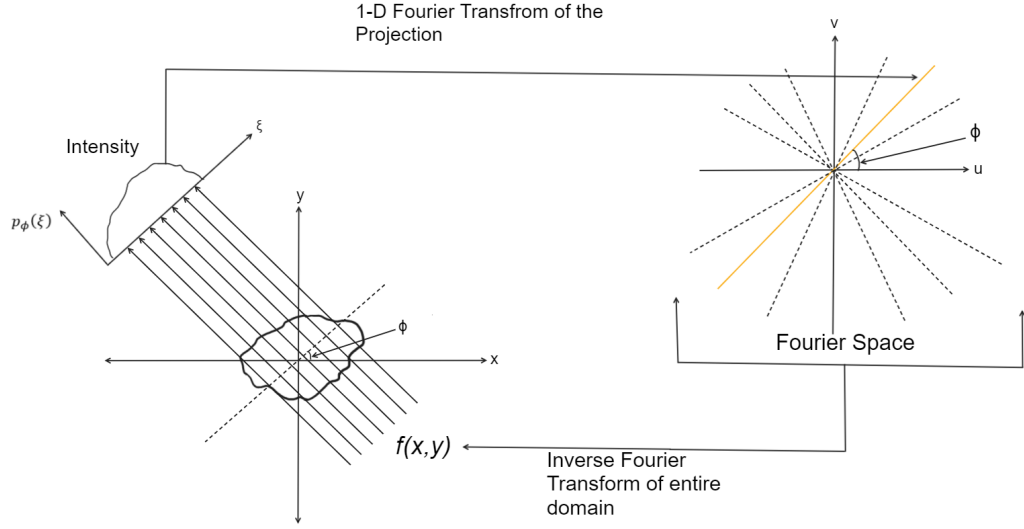


Figure 2.14: Fourier slice theorem

By observing the frequency domain, the relationship between the 1-D Fourier transforms  $p(\xi, \phi)$  of the projection function  $p_\phi(\xi)$  and the spatial function  $f(x, y)$  can be established.

$$F(u, v) = \mathcal{F}\{f(x, y)\}, \quad (2.24)$$

$$p(\xi, \phi) = \mathcal{F}\{p_\phi(\xi)\}, \quad (2.25)$$

where  $\mathcal{F}$  is the Fourier transform function. A radial line found in the Fourier domain  $F(u, v)$ , at the angle  $\phi$  along the  $u$  axis, is the 1-D Fourier transform component of  $p_\phi(\xi)$ . With enough projection numbers, the Fourier space will be filled with radial lines, then we can have a good estimate of  $F(u, v)$ . Then, performing an inverse Fourier transform on  $F(u, v)$  leads us back to the original function  $f(x, y)$  [24]. So, each projection image of the object contributes to the radial lines found in Fourier space. Figure 2.15 shows the flow of the Fourier slice theorem.

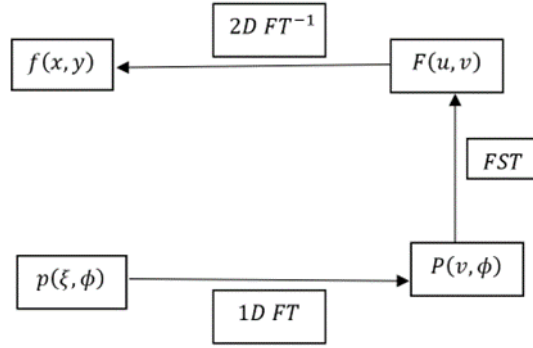


Figure 2.15: Fourier transform-based reconstruction flow

$FT$  and  $FT^{-1}$  are the Fourier transform and inverse Fourier transform, respectively. Based on the Fourier slice theorem, a commonly used reconstruction technique known as filtered back projection (FBP) is developed. Performing reconstruction in an ideal case where the X-ray radiation is parallel and monochromatic radiation is described, and is computationally simpler. With a practical scenario, the geometric setup is taken into consideration, and different reconstruction techniques are used accordingly. FBP is the basis for most of the analytical reconstruction techniques.

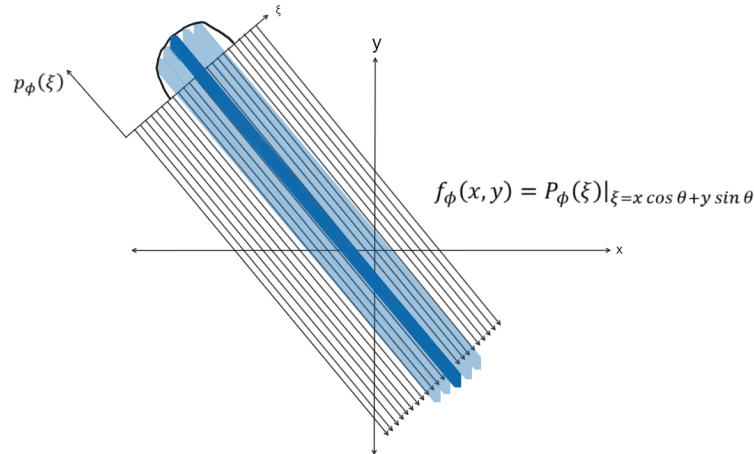
### 2.3.4 Filtered Back Projection (FBP)

To understand FBP, we need to split the concept into two. First back projection, and second filtering. We start off with back projection. The projection image is a registered image intensity profile at a certain angle. Back projecting a projection image means estimating the attenuation coefficient from the observed intensity profile. The equation below describes the scenario.

$$f(x, y) = \int_0^\pi p(x \cos \phi + y \sin \phi, \phi) d\phi, \quad (2.26)$$

Radon transform or forward projection of the object function  $f(x, y)$ , results in projection image  $p_\phi(\xi)$ . The function  $f(x, y)$  contains the attenuation coefficient of the material that is sampled in a 2-D space. The registered intensity profiles  $p_\phi(\xi)$  are mathematically back-projected to estimate the original function  $f(x, y)$ .

Back projection operation simply propagates the measured projection image back into the original image space along the projection path, or smears the line integrals, i.e.,  $x \cos \phi + y \sin \phi$  for each angle point in a projection space  $p_\phi(\xi)$ , along the lines without filtering, as can be seen in Fig. 2.16. A back projection of a single projection image, a smeared line according to the equation, hardly gives any information about the original function  $f(x, y)$ . However, when multiple/sufficient back projections are combined, the function  $f(x, y)$  can be reconstructed.


 Figure 2.16: Single-intensity image back projection hardly gives an estimate of the original function  $f(x, y)$



Simple raw back-projection for image reconstruction purposes is prone to image blurring for the final reconstructed version. Such a scenario can be explained when we look at the frequency domain of the reconstruction technique accordingly with the Fourier slice theorem as described in the previous section. As a recap, a 1D Fourier transform of the projection  $p(\xi, \phi)$  is equal to a slice, at  $\phi$ , of  $F(u, v)$  that is a 2D Fourier transform of the original function  $f(x, y)$  shown in Fig. 2.14.

Fourier slice theorem-based reconstruction process is:

1. Collect a projection image of the object being scanned (with a specific angular sampling)
2. Rearrange the projections into sinogram (projection function of angle)
3. Add those projections in Fourier space by doing a 2-D Fourier transform.
4. 2-D Inverse Fourier transforms the collected total projection to the spatial domain to get the reconstructed image.

Figure 2.17 shows angular sampling in the frequency domain, with radial lines being the projections. It can be seen that there is a higher data sample in the middle (close to the origin) while ones further away from the origin are relatively under-sampled. This means more sampling is done for lower frequency values, while higher frequency is under-sampled which is the main reason behind the blurring during back-projection operation.

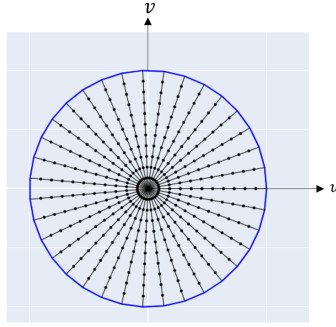


Figure 2.17: Frequency domain sampling/polar sampling

Filtered back projection (FBP) reduces the blurring effect by using a ramp filter, which dampens lower-frequency components while enhancing higher-frequency values. Different types of ramp filters are available, and their selection depends on the trade-off between achieving a smooth image or a higher spatial resolution [25].

FBP is used to solve the inverse Radon transform by back-projecting using the Fourier slice theorem (FST) method and applying ramp filters to reduce blurring. The mathematical procedure for FBP is shown below:

$$f(x, y) = \int_0^\pi \int_{-\infty}^{\infty} p(\omega, \phi) e^{-j2\pi\omega(x \cos \phi + y \sin \phi)} |\omega| d\omega d\phi, \quad (2.27)$$

$$f(x, y) = \int_0^\pi p'(x \cos \phi + y \sin \phi, \phi) d\phi, \quad (2.28)$$

$$p'(\omega, \phi) = \int_{-\infty}^{\infty} |\omega| p(\omega, \phi) e^{-j2\pi\omega(x \cos \phi + y \sin \phi)} d\omega, \quad (2.29)$$

In these equations, the term  $|\omega|$  represents an unlimited ramp filter where the higher frequency limit is not specified (i.e., it is not clipped). To avoid amplifying projection noise during filtering, higher frequency terms need to be limited.  $|\omega|$  can be replaced by an arbitrary filter  $H(\omega) = |\omega|$ , resulting in:

$$p'(\omega, \phi) = \int_{-\infty}^{\infty} p(\omega, \phi) H(\omega) e^{-j2\pi\omega(x \cos \phi + y \sin \phi)} d\omega, \quad (2.30)$$

where  $p'(\omega, \phi)$  is filtered projection image. The filtering process can be done either by performing multiplication in the Fourier domain or by carrying out convolution operations in the spatial domain. The most commonly used filters are the Ram-Lak filter and Shepp logan [25], their frequency domain plot is shown in the figure below.

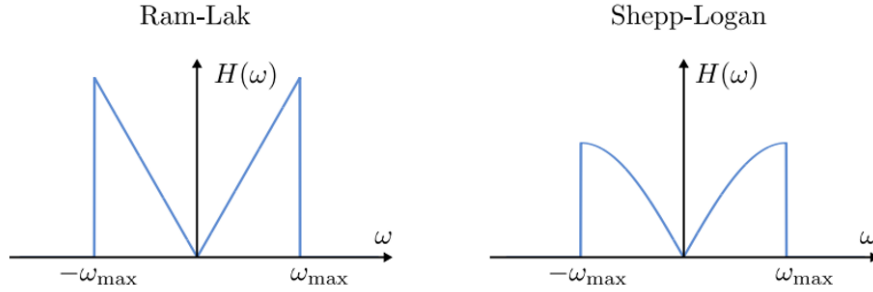


Figure 2.18: Commonly used ramp filters during filtered back projection reconstruction

The basics of reconstruction have taken into account a perfectly parallel beam geometry and a 2-D space for the sake of simplifying the mathematical explanation. During the work of the thesis project, the X-ray system uses a cone-beam setup. Reconstruction in such scenarios needs to take the geometric setup into consideration. This makes analytical CT reconstruction sensitive to any geometric inaccuracies and the reconstruction can produce incorrect results. Figure 2.19 shows the commonly used setups for X-ray CT scanning.

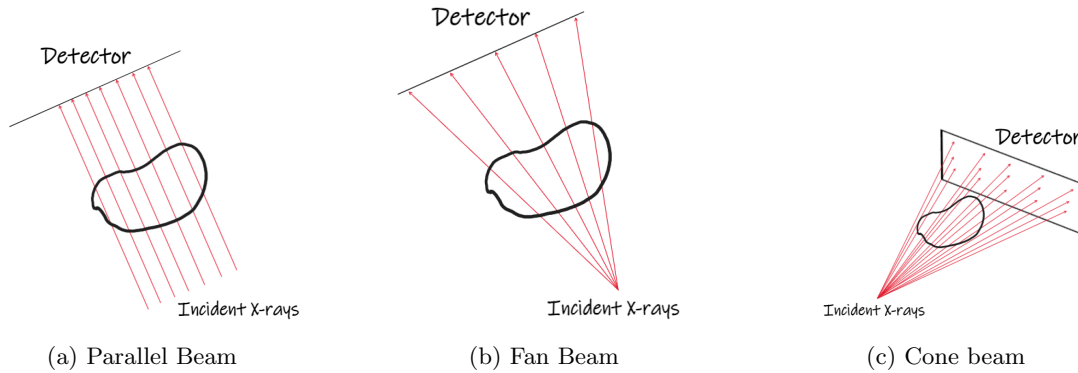


Figure 2.19: Commonly used geometric setups for X-ray CT scanning

By taking the geometrical setup into consideration, the filtered back projection can be modified to create a new reconstruction algorithm. The next section covers such cases when the geometry is for a cone-beam setup and on which the thesis project is based.

### 2.3.5 Feldkamp-Davis-Kress (FDK) Reconstruction

According to [26], there are four families of reconstruction algorithms. One of them is the filtered back projection, this algorithm is the solution to the inverse Radon transform problem, and it was covered in the previous section. One of the most widely used reconstruction algorithms for cone beam setup is the FDK, named after the authors. In 1984, Feldkamp, Davis, and Kress introduced the FDK algorithm as a means to reconstruct cone-beam projections obtained from circular orbits of the X-ray source around an object [27], enabling three-dimensional reconstruction.

In the case of cone-beam setup, the principle of tomography is the same as discussed before. A 2-D X-ray image of the sample is taken from different angles, and a reconstruction algorithm is used to reconstruct the volumetric (3-D) image of the sample. For analytical reconstruction, it is similar to the inverse Radon problem, what differs is that we have to factor in the geometry when doing back projection, and our math changes to a 3-D space. However, reconstructing cone-beam images is much more difficult compared to the reconstruction of parallel line-integral and parallel

plane-integral data [28]. Compared to the parallel projection that was discussed in the previous section, in the case of cone-beam images, there is no known equivalent central slice theorem, which makes it not a straightforward process. The coordinate system for an FDK algorithm in cone-beam setup can be seen in Fig. 2.20

The general procedure for FDK reconstruction generally takes similar steps most of the time as was shown in [29, 5, 28] mainly for circular cone beam computed tomography (CBCT) since it is an analytical method. Differences may arise in the geometric setup as was shown in [29], where they look into modified versions of FDK to have a better reconstruction quality for higher cone-beam angles, as the quality of reconstruction deteriorates with increasing cone-beam angle but the main principle is the same. The steps are:

1. Weighting the projection data based on geometry, which involves applying a pre-weighting factor that corresponds to the cosine of the angle  $\beta$  between the cone-beam ray passing through the reconstruction point and the central ray of the projection.
2. Applying ramp filter row by row on the image pixel to the pre-scaled function in step 1.
3. Back-project the filtered projection by a weighting function of the distance between the focal point (source) to the reconstruction point.

The pre-weighting factor is given by:

$$\frac{D}{\sqrt{D^2 + x'^2 + z'^2}}, \quad (2.31)$$

Where  $D$  is the focal length,  $(x', z')$  are the spatial coordinates on the flat panel detector representing the pixel positions. The FDK reconstruction considers that the source and detector are rotating along the  $z$ -axis reference frame of the volumetric object specified by the  $(x, y, z)$  coordinates [27] as shown in Fig. 2.20. This is similar to the object rotating while the source and detector are stationary.

$$\tilde{p}(x', z', \beta) = \left( \frac{D}{\sqrt{D^2 + x'^2 + z'^2}} \cdot p(x', z', \beta) \right) \star h(x'), \quad (2.32)$$

where  $\star$  represents the convolution operation in the spatial domain.  $p(x', z', \beta)$  is a function that represents the raw projection data collected at a projection angle of  $\beta$  on the pixel coordinates  $(x', z')$ . This dataset requires filtering using ramp filters, and  $\tilde{p}(x', z', \beta)$  is the projection data after pre-weighting and filtering using a ramp filter  $h(x')$ . The filtering is done along the row direction.

$$f(x, y, z) = \int_0^{2\pi} \frac{D^2}{(D + x \sin \beta + y \cos \beta)^2} \left( \frac{D}{\sqrt{D^2 + x'^2 + z'^2}} \cdot \tilde{p}(x', z', \beta) \right) d\beta, \quad (2.33)$$

where  $f(x, y, z)$  is the final reconstructed volume along the 360-degree rotation. The location of the data point being reconstructed as a function of  $\beta$  can be found in the reconstruction point coordinates  $f(x, y, z)$  as

$$x'(x, y, \beta) = \frac{D(-x \sin \beta + y \cos \beta)}{D + x \cos \beta + y \sin \beta}, \quad (2.34)$$

$$z'(x, y, z, \beta) = \frac{zD}{D + x \cos \beta + y \sin \beta}, \quad (2.35)$$

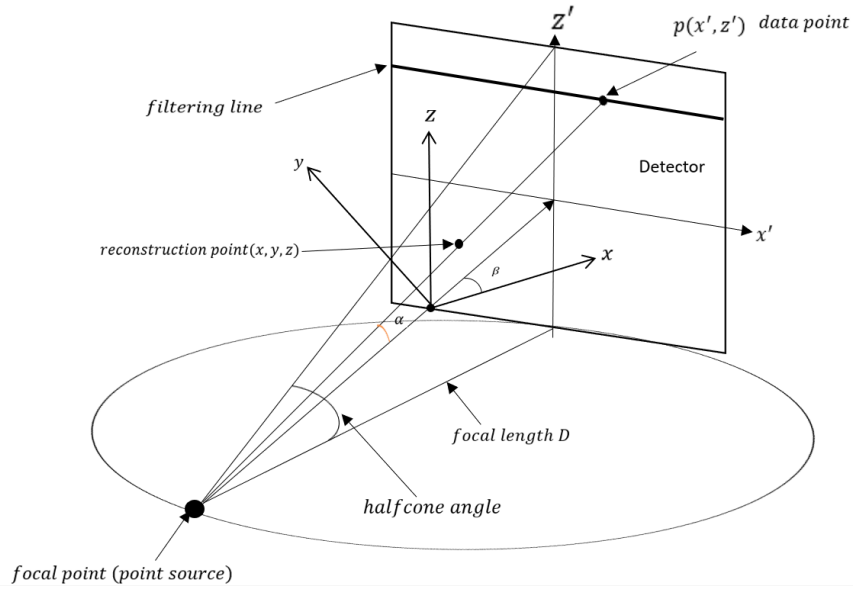


Figure 2.20: Coordinate system for FDK algorithm for a circular cone-beam geometry. A point of the reconstructed object is taken along its  $xyz$  coordinates, while the detector registers the data on the specified pixel coordinates  $(x', z')$ . An instance of rotation is shown where the source and detector have rotated at an angle of  $\beta$

## 2.4 Image Quality

Assessing the quality of an image can be done in different ways, from simple visual check (qualitative analysis) to quantitative analysis using signal-to-noise ratio (SNR) or contrast-to-noise ratio (CNR). In X-ray imaging, the three most important properties according to [7] are contrast, noise level, and resolution. Figure 2.21 illustrates these three properties. The three properties combined can be used as image quality metrics to calculate the SNR and CNR in comparing tomographic images.

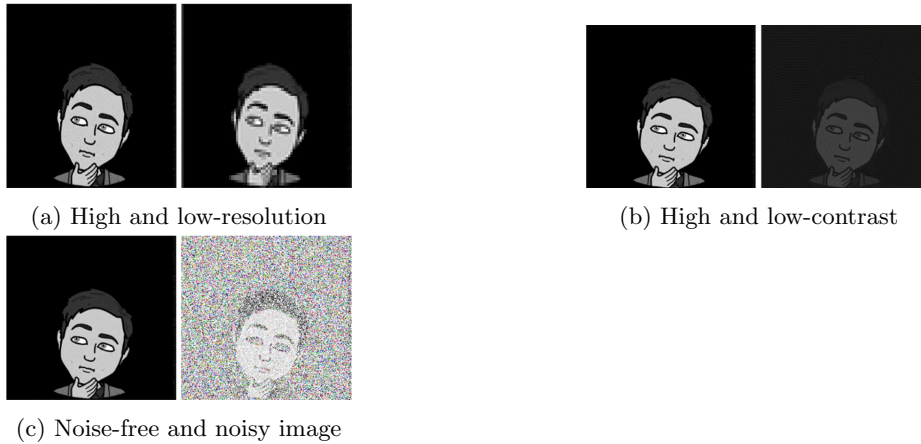


Figure 2.21: Illustration of resolution, contrast, and noise

Contrast is the difference in the intensity of the image/pixel relative to the background. In higher-contrast images, the detailed features of the image can easily be seen. The resolution of an image indicates how fine and small details can be seen. If we have a low-resolution image, it will be blurred with pixelated image, while the high-resolution image looks sharper and finer details are represented. The pixel size and magnification during X-ray imaging affect resolution. Noise is an unwanted property in an image, and there are different noise sources for X-ray imaging. Many of the

noise types can be modeled as Gaussian, for example, it was used for signal-to-noise ratio analysis in [8] and by [7] during simulation modeling of X-ray detectors. Photon noise is a common type of noise in X-ray imaging. This occurs due to the quantized nature of light reaching the detector [7].

# Chapter 3

## Methods

In this chapter, the process followed to perform helical scanning, data processing are covered. The usage of the Paganin phase retrieval method as a low-pass filter on a poorly contrasting biological sample is also shown.

### 3.1 X-ray Micro-CT Laboratory Setup

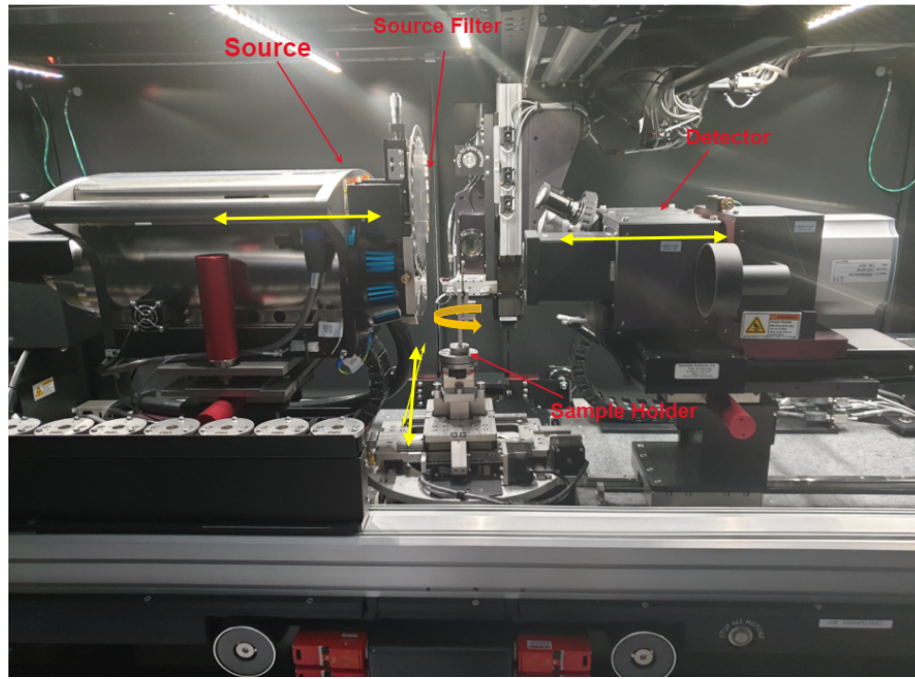
The experiment was performed with a commercial micro-CT machine, i.e., Zeiss Xradia Versa 520 at Stockholm University Brain Imaging Centre (SUBIC). Micro-CT systems can be used by researchers for advanced material research and development, in semiconductor package development and failure analysis, geo-materials physics modeling, oil and gas exploration, and many other research and industrial fields.

A photo of the main components of the X-ray micro-CT scanner and its direction axes is shown in Fig. 3.1, which consists of sensitive mechanical, optical, and electronic components. The X-ray machine has software for data acquisition and processing. One can also create an experimental data acquisition script by application programming interface (API) using Python.

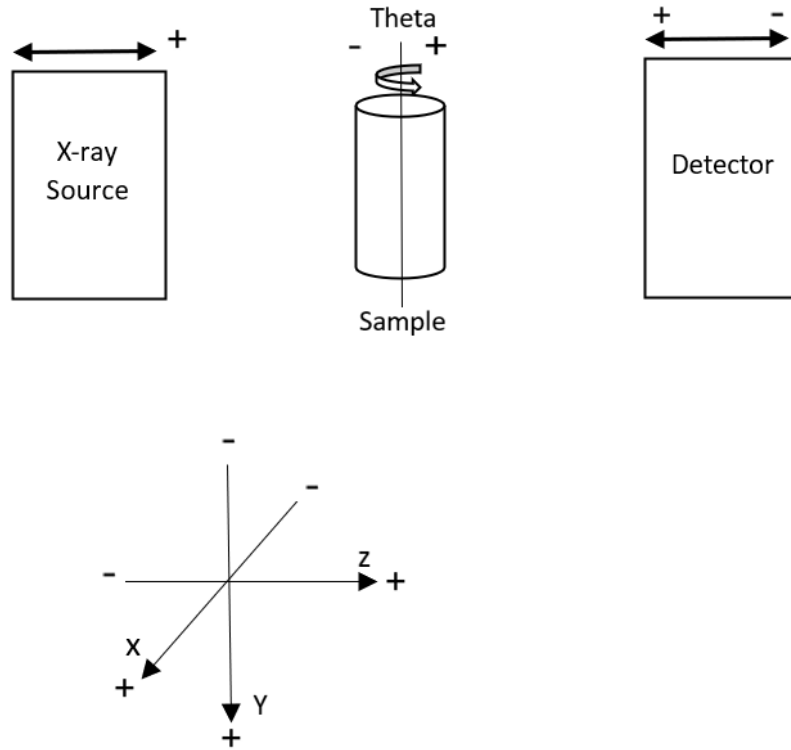
The X-ray source is micro-focused. It contains a filter holder, where the user can choose between different filters, to produce a better-filtered X-ray energy spectrum. The filters are grouped between high-energy and low-energy filters [30]. These filters serve the purpose of eliminating low-energy X-rays that can be mostly absorbed by the sample but do not contribute to image contrast. Their primary function is to improve the overall image quality by selectively removing undesired X-rays. The source input voltage ranges from 30-160 kV, with a maximum power of 10W [30].

The detector is an indirect type of detection, where a scintillator-based, and lens-coupled CCD detector is used to capture the incoming X-rays and convert them into an electrical signal. The scintillator absorbs the X-ray images and converts them into visible light, which is focused by the lens onto the CCD detector. As seen from Fig. 3.1a, the detector assembly holds motorized turrets and objectives, that can be switched to different sets of optical magnifications 0.4x, 4x, 20x, and 40x.

The sample holder assembly has four degrees of freedom, with a motorized precision movement capable of moving along the xyz direction, and full rotation along the y-axis. This movement is used to align the object to the field of view (FOV) of the objective.



(a) Main components of the micro-CT Scanner



(b) Movement axis

Figure 3.1: Directions when the sample theta stage is at 0 degrees: The z and x axes rotate with the sample stage. When the sample theta stage is set to -90 degrees, the z-axis moves perpendicular to the beamline, while the x-axis moves parallel to the beamline

## 3.2 Helical Data Acquisition and Pre-Processing

The helical scanning technique in a micro-CT setup departs from the conventional method where the sample is only rotated during tomographic image acquisition. Helical scanning introduces vertical translation movement to extend the field of view (FOV) of the scan. This extension accommodates elongated samples that wouldn't fit within the standard FOV. To perform helical scanning, an object with an elongated length that doesn't fit fully on the detector FOV is selected. With known material composition and uniform material structure, a pencil made out of basswood and graphite with a dimensional specification of 7 mm×190 mm is used. From Fig. 3.2 the placement of the sample (pencil) is shown. It was mounted on an aluminum sample holder and is tightly secured to reduce mechanical instability during the rotation and translation stage.

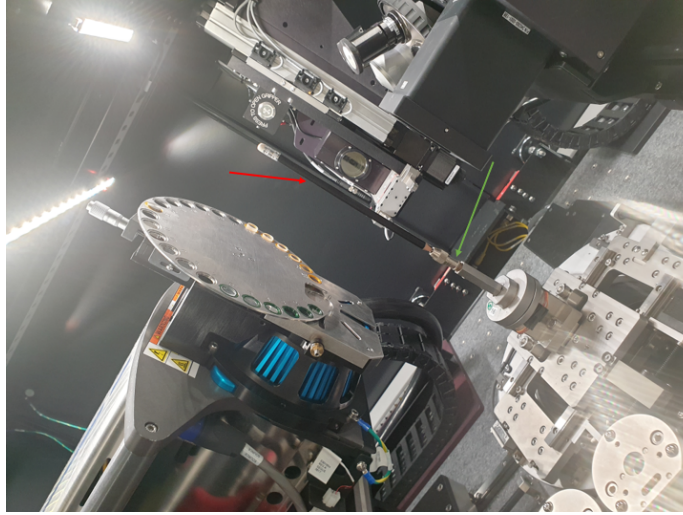


Figure 3.2: Mounting of the scanned sample on the micro-CT scanner for helical data acquisition. The red arrow indicates the pencil and the green arrow indicates the sample holder for mechanical stability.

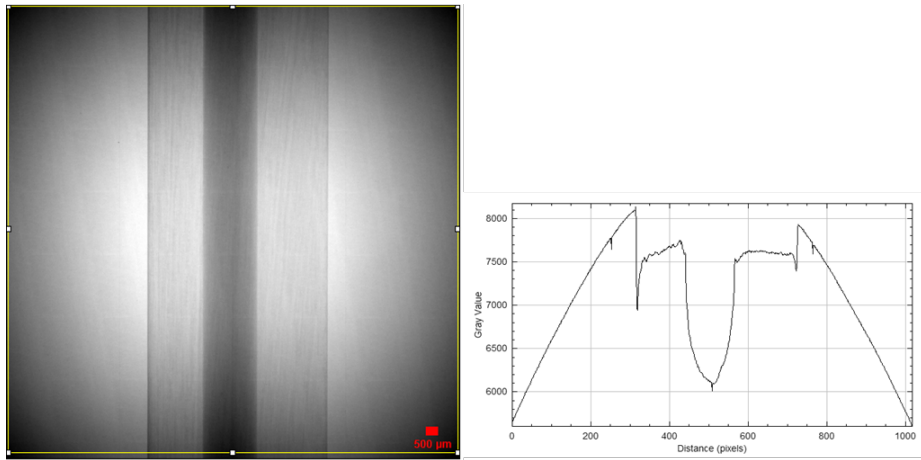
For a full 360-degree scan, 800 projections were taken, with an angular increment of  $0.45^\circ$  and a vertical translational increment of 0.05 mm per projection. Each projection was exposed for 1 second, and the acquired projection was binned by a  $2 \times 2$  pixel window, leading to a raw projection image size of  $1024 \times 1024$  pixels. The binned detector's effective pixel size is  $17.63 \times 17.63 \mu\text{m}^2$  for a total detector field of view of  $18.056 \times 18.056 \text{ mm}^2$ . The source voltage and power were set to 80 kV and 7 W respectively during the experiment. The parameters were chosen to ensure good contrast in the projection space. Table 3.1 summarizes the parameters used.

Table 3.1: Helical data acquisition parameters

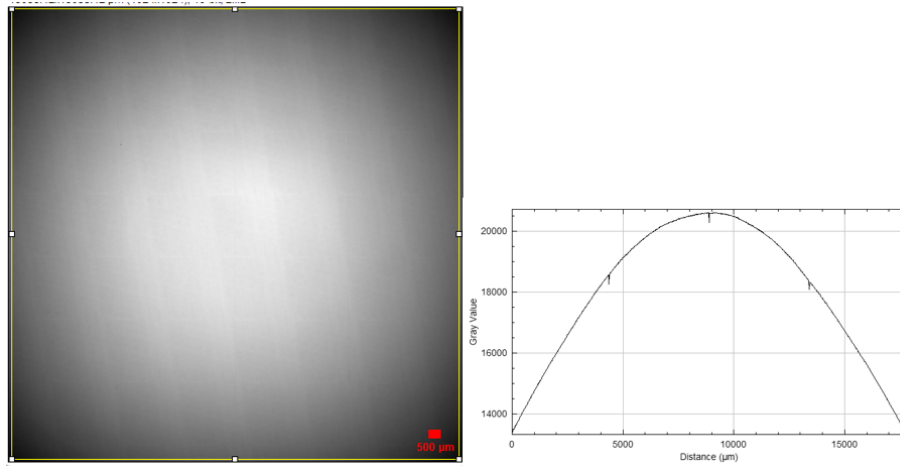
Parameter	Value
Tube Voltage	80 kV
Power	7 W
Sample Exposure	1 sec
Binning	$2 \times 2$
Effective Detector Pixel Size	$17.63 \mu\text{m}$
Detector Effective FOV	$18.056 \times 18.056 \text{ mm}^2$
Pixel Width $\times$ Pixel Height	$1024 \times 1024$
Source to Sample Distance	53.53 mm
Sample to Detector Distance	153.38 mm
Objective	0.4 $\times$
Geometric Magnification	3.87
Total Projection	800
Total Pitch	40 mm
Cone Angle	9.570
Angular Sample	0.450
Pitch per Projection	0.05 mm



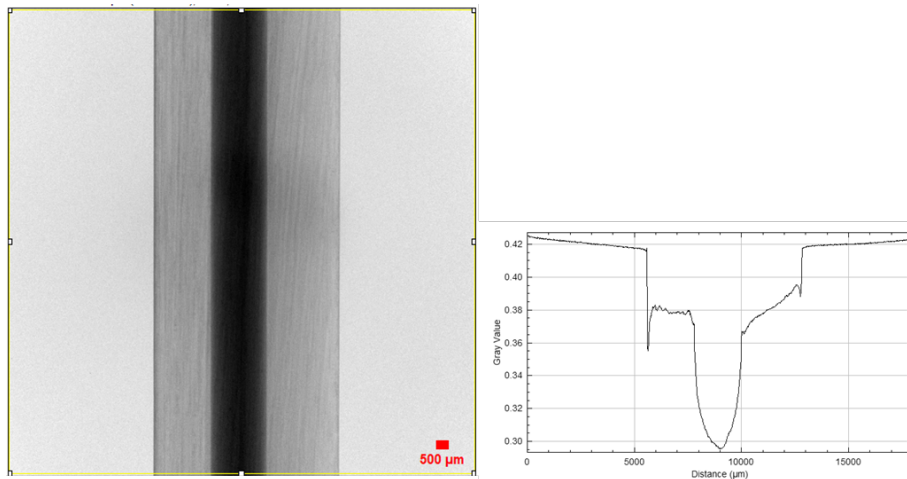
Before starting the acquisition, while the X-ray source is turned off an image is taken, it is called a dark frame. The dark frame image records the detector's inherent offset count. The initial factor requiring correction is known as the "dark current" of the detector. The dark current is an electronic phenomenon leading the detector pixels to register values other than zero, even in the absence of X-ray photon impact. Then X-ray source is switched on and the sample is moved out of the FOV to take another projection image called a flat-field image. The flat-field image records the X-ray beam intensity profile distribution and is used to determine the response of the imaging system. In an ideal case, it is expected to get a perfectly homogeneous intensity profile registration for flat-field images, but that isn't the case in reality. The flat-field image is used to correct the factor of the X-ray source intensity being non-homogenous. The flat-field and dark frame images are used for pre-processing i.e., flat field correction, where the original raw X-ray projection image undergoes correction to account for fluctuations in X-ray source intensity and variations in detector sensitivity. The corresponding raw-projection image, flat field image, and corrected image with their respective intensity profile plot and dynamic range are shown in Fig. 3.3.



(a) Raw X-ray projection image of a pencil with a dynamic intensity range of [4043, 9530] and its intensity profile plot.



(b) Flat-field image with a dynamic intensity range of [9079, 2482] and its intensity profile plot.



(c) Flat-field and dark-frame corrected image with a dynamic intensity of [0, 1] and its intensity profile plot.

Figure 3.3: Example of collected projection images taken with their respective intensity profile plot and dynamic range. The flow shows the flat-field correction stage from the first row to the last. Intensity profile plots are taken from the yellow box region.

The flat-field correction is done by:

$$X = \frac{P - D}{F - D} \quad (3.1)$$

Where  $P$  is the raw X-ray image,  $D$  is the dark frame image, and  $F$  is the flat-field image. The flat-field and dark corrected image  $X$  shows the X-ray attenuation after traversing through the object being scanned.

Based on Beer-Lambert's equation, as shown in Equation (2.18), the following equation relates the intensity of the X-ray, denoted as  $I(s)$ , to the density of the object,  $\mu(s)$ , where  $s$  is the distance traveled through the object:

$$I(s) = I_0 e^{-\int_0^s \mu(x) dx} \quad (3.2)$$

$$p(s) = -\ln\left(\frac{I}{I_0}\right) = \int_0^s \mu(x) dx \quad (3.3)$$

Here,  $p(s)$  represents the projection image, and the value of each pixel corresponds to the sum of density i.e.  $\int_0^s \mu(x) dx$  along the X-ray beam passing through the object. To prepare the X-ray images for tomographic reconstruction, the ratio of photons that arrive at the detector to those produced by the X-ray source is calculated, and the negative natural logarithm of this ratio is taken. Here,  $I$  represents the flat-field and dark frame-corrected image, which represents the beam intensity loss image ( $X$ ), and  $I_0$  is the incident X-ray represented by the reference image ( $F$ ).

The resulting projection image is shown in Fig. 3.4 with its intensity plot. The process is done for each projection image out of the total 800, with the help of a Python script.

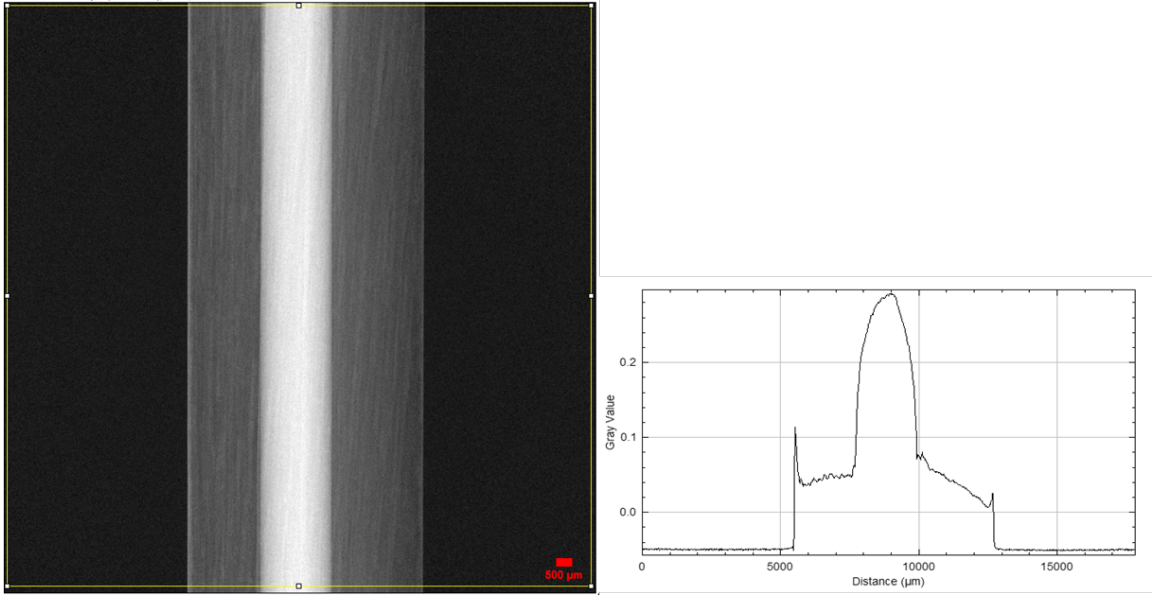


Figure 3.4: The projection image is prepared for reconstruction, by taking the negative logarithm of the flat-field corrected image and its corresponding profile plot.

Helical motion is produced by rotating and translating the sample along its rotational axis and is used to increase the FOV of the detector unit vertically by including parts of the sample that are large enough to be within the FOV. Figure 3.5 describes the overview of the helical scan data acquisition. By taking the tomographic images and adding translational motion along the vertical axis, part of the sample that is outside of the FOV can be scanned and reconstructed. The micro-CT scanner's data acquisition software doesn't allow scanning techniques other than the conventional scheme where the sample only rotates, and projection images are taken but it offers an application program interface (API) for Python scripting. The API enables for instrument control API module which one can have access to functions to engage with the X-ray microscope, allowing actions like motor movement and objective adjustments. In order to perform helical scanning, the instrument

control API module was used and Python script to control the motion and collect angular and translational position of the sample while taking projection images.

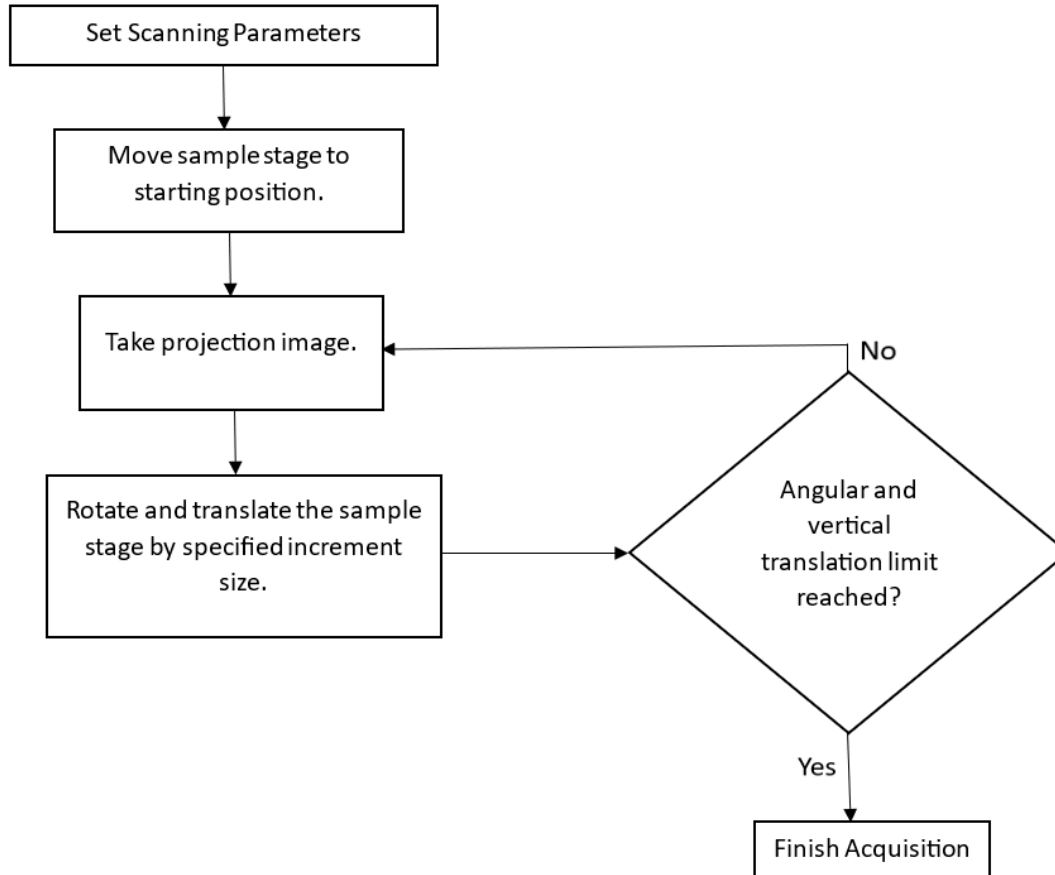


Figure 3.5: The overall flow of the helical scanning technique.

This experimental setup was designed to include the region of interest of the sample that lies outside of the FOV using the helical scanning technique. Figure 3.6 demonstrates how the FOV determines the area of the sample to be scanned. Part of the object that is outside of the FOV cannot be scanned when using the conventional micro-CT rotational scanning technique unless two vertical stitching scans are taken.

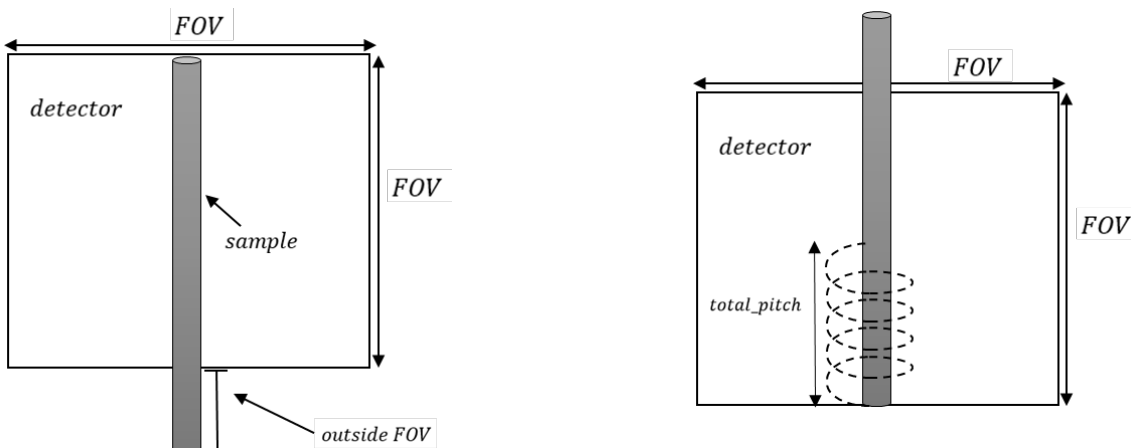


Figure 3.6: Demonstration of the sample outside of FOV

A snapshot of the projection of the scanned sample is shown below in Fig. 3.7. With specified scanning parameters shown in Table 3.1, the maximum length of the pencil that can be scanned is 18.056 mm.

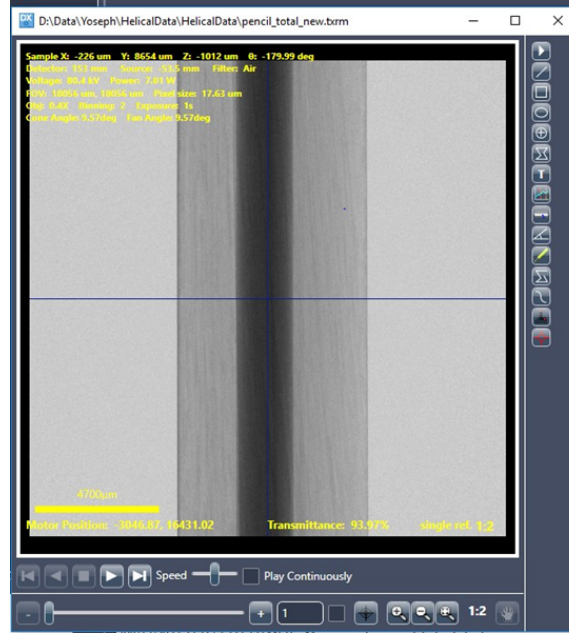


Figure 3.7: One projection image of a pencil where the entire vertical FOV is fitted.

The tomographic reconstruction of the helical data was implemented using ASTRA toolbox [4]. ASTRA supports different X-ray scanning geometries. By using the ASTRA toolbox it is possible to specify each projection image's geometric position during the data acquisition by the scanner and can be reconstructed accordingly. ASTRA toolbox assumes that the object being scanned is stationary, and both the source and the detector rotate perfectly around the z-axis when using a conventional cone-beam CT geometric specification or by using vector-based geometric specification where the parametrization is shown in the figure below, it is possible to model a flexible scanning geometry.

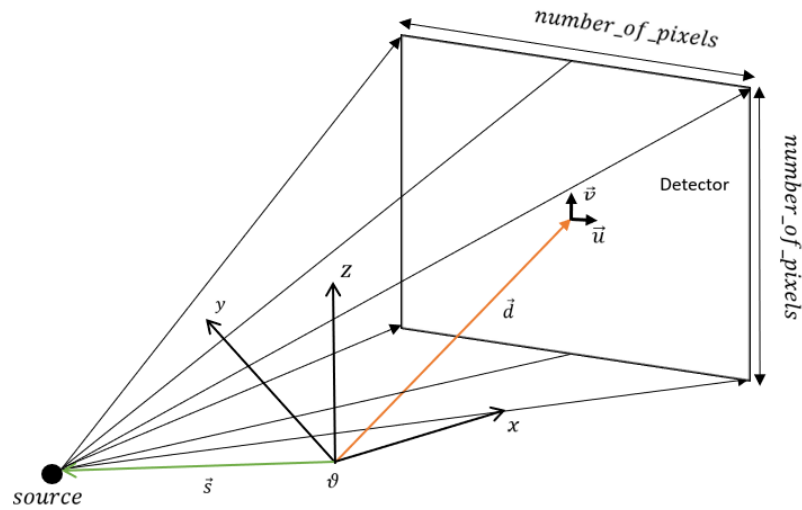


Figure 3.8: Parametrization of cone-beam geometry scanning in ASTRA Toolbox.

Vector-based geometric specifications such as source position  $\mathbf{s} = (x, y, z)$  relative to frame  $\theta$ ,

detector center position  $\mathbf{d} = (x, y, z)$  relative to frame  $\vartheta$ , and detector principal axes given by the unit vectors  $\mathbf{u} = (u_x, u_y, u_z)$  and  $\mathbf{v} = (v_x, v_y, v_z)$ , with the length of the vectors being the effective pixel size of the detector. The projection geometry is created as a  $n \times 12$  matrix format where  $n$  is the number of projections. Each row describes the projection geometry for the specified projection number:

$$\begin{array}{cccccccccccc} s_{x1} & s_{y1} & s_{z1} & d_{x1} & d_{y1} & d_{z1} & u_{x1} & u_{y1} & u_{z1} & v_{x1} & v_{y1} & v_{z1} \\ \vdots & \vdots & \vdots & \vdots & \vdots & \vdots & \vdots & \vdots & \vdots & \vdots & \vdots & \vdots \\ s_{xn} & s_{yn} & s_{zn} & d_{xn} & d_{yn} & d_{zn} & u_{xn} & u_{yn} & u_{zn} & v_{xn} & v_{yn} & v_{zn} \end{array}$$

By following the vector-based parametrization using the ASTRA toolbox, the helical scanning geometry modeling is shown in the figure below with an appropriate mathematical description.

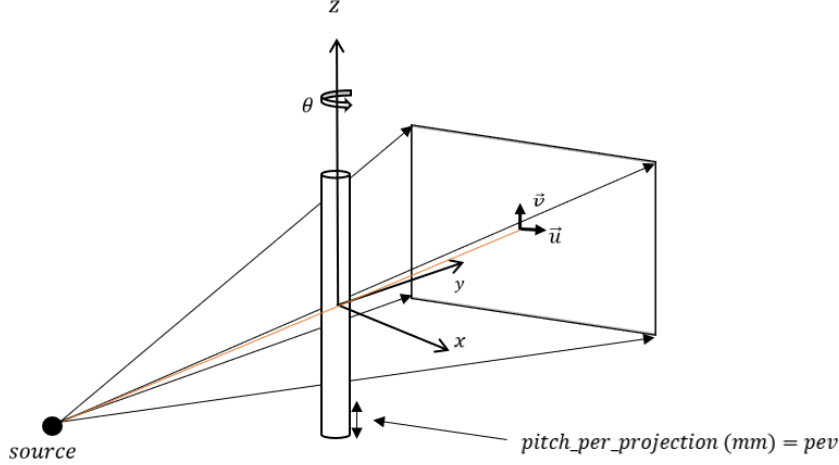


Figure 3.9: Helical scan modeling according to the ASTRA toolbox cone-beam geometric parametrization.

Taking the fixed coordinate system  $(x, y, z)$  where the central ray (orange line) crosses towards the center of the detector, the positions of the vectors are given as (assuming a stationary position):

$$\mathbf{s} = (0, -s, 0), \quad \mathbf{d} = (0, d, 0), \quad \mathbf{u} = (u, 0, 0), \quad \mathbf{v} = (0, 0, v)$$

where  $s$  and  $d$  are the source and detector distances along the optical axis  $y$ , and  $u$  and  $v$  are the effective pixel sizes.

In order to describe the helical scanning geometry, the source and detector rotate around the  $z$ -axis and translate  $pev$  amount per rotation along the same axis, while the sample being scanned is stationary. The new vector position of each coordinate can be described by simply multiplying them with a rotation matrix along the  $z$ -axis, given by

$$R_{iz} = \begin{bmatrix} \cos \theta_i & -\sin \theta_i & 0 \\ \sin \theta_i & \cos \theta_i & 0 \\ 0 & 0 & 1 \end{bmatrix}$$

$$\mathbf{s}'_i = R_{iz} \mathbf{s}_i, \quad \mathbf{d}'_i = R_{iz} \mathbf{d}_i, \quad \mathbf{u}'_i = R_{iz} \mathbf{u}_i, \quad \mathbf{v}'_i = R_{iz} \mathbf{v}_i$$

where  $i$  is the projection number.

The translation increment value produced by the sample stage motor  $pev$  is related to the projection translation at the detector unit by taking the effective pixel size dimension unit along the  $z$ -axis (i.e.,  $\mathbf{v} = (0, 0, v)$ ) into account. The final equations are given below:

$$\begin{aligned} \mathbf{s}'_i &= R_{iz} \mathbf{s}_i + pev R_{iz} \mathbf{v}_i \\ \mathbf{d}'_i &= R_{iz} \mathbf{d}_i + pev R_{iz} \mathbf{v}_i \\ \mathbf{u}'_i &= R_{iz} \mathbf{u}_i \\ \mathbf{v}'_i &= R_{iz} \mathbf{v}_i \end{aligned}$$

$$\text{where } \mathbf{s}'_i = \begin{bmatrix} -s \sin \theta_i \\ s \cos \theta_i \\ \text{pev} \cdot v \end{bmatrix}, \mathbf{d}'_i = \begin{bmatrix} -d \sin \theta_i \\ d \cos \theta_i \\ \text{pev} \cdot v \end{bmatrix}, \mathbf{u}'_i = \begin{bmatrix} u \cos \theta_i \\ u \sin \theta_i \\ 0 \end{bmatrix}, \text{ and } \mathbf{v}'_i = \begin{bmatrix} 0 \\ 0 \\ v \end{bmatrix}.$$

For helical scanning with a detector effective FOV of  $18.056 \times 18.056 \text{ mm}^2$ , a total pitch of 40 mm results in 58 mm FOV vertically. In order to make a comparison with the helical scan, a conventional tomographic scan that produces vertical FOV as close to 58 mm as possible is done. This setup is used so as to increase the FOV in scanning the pencil but without using the helical scanning technique. This is done by placing the source at -212.95 mm and the detector at 49.014 mm which results in a FOV of  $56.736 \times 56.736 \text{ mm}^2$ . The resolution, FOV, and pixel size are affected by the source and detector distance from the sample. The selection of the X-ray source and detector distance from the sample so as to increase the FOV is based on the following relationship and is summarized in the figure below.



Figure 3.10: Illustration of how FOV is affected by the X-ray source and detector distance placement from the scanned sample.

The same experimental parameters are set, with the exception of the detector and source position. With exposure time per projection of 1 second, and hardware binning of  $2 \times 2$  resulting in projection image dimensions of  $1024 \times 1024$  pixels. For a full 360-degree rotation, 800 projections were taken in total. The source voltage and power were set to 80 kV and 7 W respectively. Table below summarizes the scan parameters for the conventional tomographic scan.

Table 3.2: Conventional scan data acquisition parameters.

Tube Voltage	80 kV
Power	7 W
Sample Exposure	1 sec
Binning	$2 \times 2$
Effective Detector Pixel Size	55.40 $\mu\text{m}$
Detector Effective FOV	$56.736 \text{ mm} \times 56.736 \text{ mm}$
Pixel Width x Pixel Height	$1024 \times 1024$
Source to Sample Distance	212.95 mm
Sample to Detector Distance	49.014 mm
Objective	0.4 $\times$
Geometric Magnification	1.23
Total Projection	800
Cone Angle	7.580
Angular Sample	0.450

The same procedure is followed for flat-field correction, and after pre-processing, the projection image to be reconstructed is shown below.

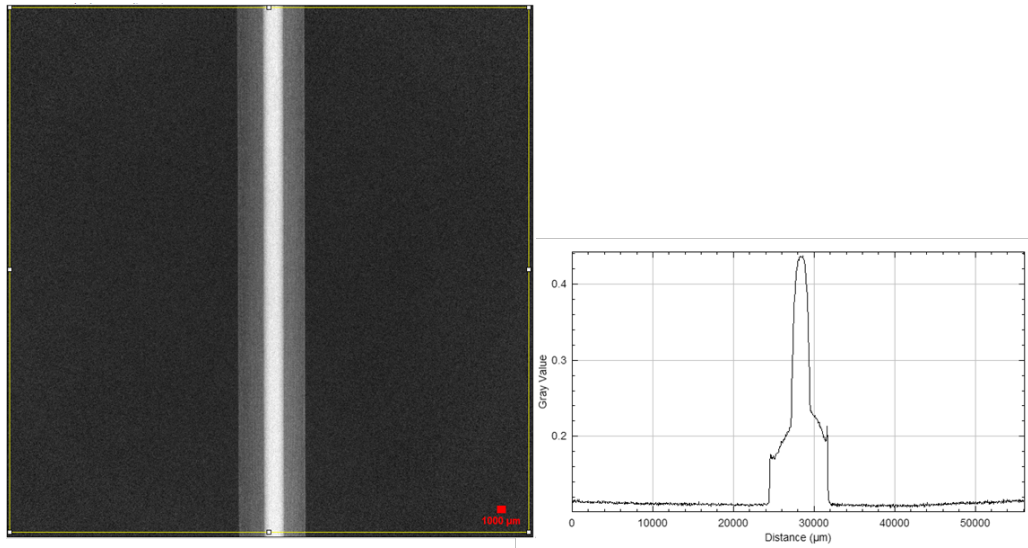


Figure 3.11: Conventional scan projection image for reconstruction and its corresponding profile plot for the entire projection. The dynamic intensity range is  $[0, 1]$ .

The reconstructed projection is placed inside a volume geometry specified by the ASTRA toolbox. This volume geometry is used to hold the attenuation coefficient values in a 3-D space, and its dimensions are set by voxel size, which is the equivalent term to pixel but in 3-D. An isometric voxel size where each dimension is equal is used during the reconstruction of both helical tomographic data and conventional scan data. The figure below shows the illustration of volume data, with axes direction based on the ASTRA toolbox convention. Reconstructed slices are stored along the z-axis plane, while the x and y axes are its dimensions.

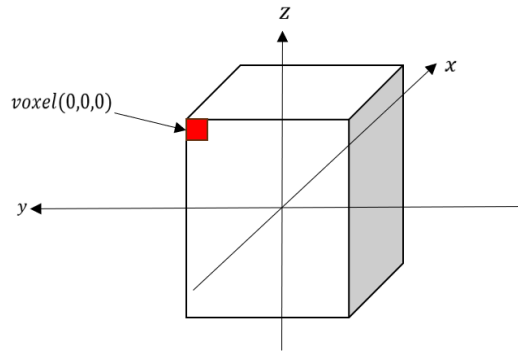
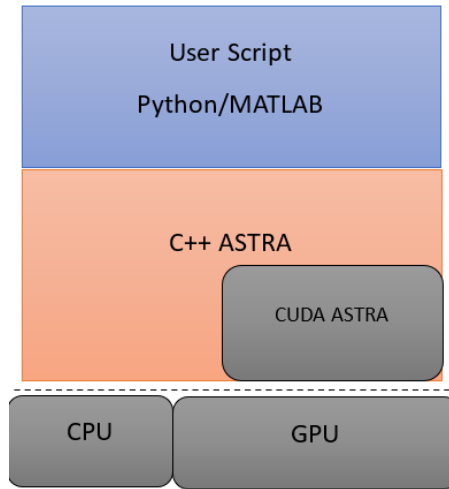


Figure 3.12: Volume geometry convention in Astratool box. Voxel sizes are set with equal dimensions on all sides.

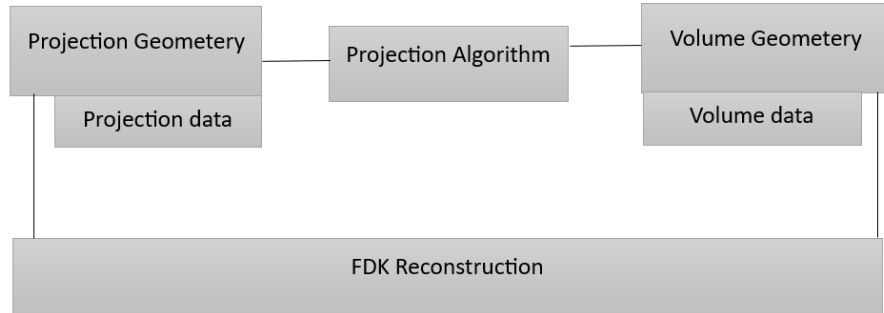
For the helical scan, a volume geometry capable of holding the reconstructed data is chosen, with dimensions of  $501^3$  and a voxel size of  $0.01\text{ mm}$ . In the case of the conventional scan, the volume size remains the same, but the voxel size is adjusted to  $0.055\text{ mm}$ . The choice of voxel size is based on the effective pixel size value.

The pre-processed projection data are linked with the modeled projection geometry and the reconstruction algorithm is chosen. In order to access different features of the ASTRA toolbox, its architectural setup is shown in Fig. 3.13, for this project, Python programming language is used to access features of the ASTRA toolbox, i.e. modeling the helical scanning geometry and FDK reconstruction algorithm.





(a) ASTRA toolbox architecture. The lower-end Graphics processor unit (GPU) accelerated reconstruction algorithm (FDK ) can be accessed with the help of Python or MATLAB.



(b) Projection geometry is linked with the pre-processed projection data, and volume geometry is linked with empty space volume data to hold the reconstructed slices.

Figure 3.13: ASTRA toolbox programming interface architecture and reconstruction concept.

The Python API script for helical scanning is provided in Appendix C. After data acquisition, the next step is pre-processing the projections, which involves using flat-field and dark-frame images. These pre-processed projection images are then linked to ASTRA's programming interface architecture to perform the FDK reconstruction algorithm. The script developed for this purpose can be found in Appendix D.

### 3.3 Phase Retrieval Method for Contrast Enhancement

As indicated in the theory section, phase retrieval becomes necessary for weakly attenuating imaged samples as enough features may be difficult to identify or segment. The Paganin phase retrieval/filter is used in this case to enhance the contrast on an example of an insect sample that was scanned at SUBIC and shown in Fig. 3.14. The insect has weak absorption but strong phase contrast showing sharp edge enhancement. However, it is very difficult to segment the volumes from intensity thresholding as the dried exoskeleton has basically the same grey level as the air (background).

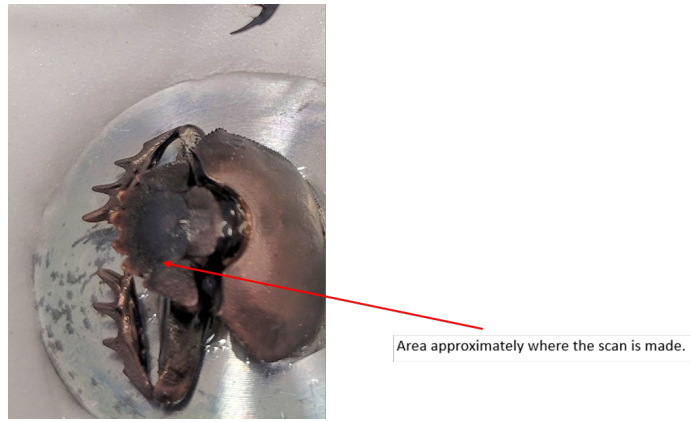


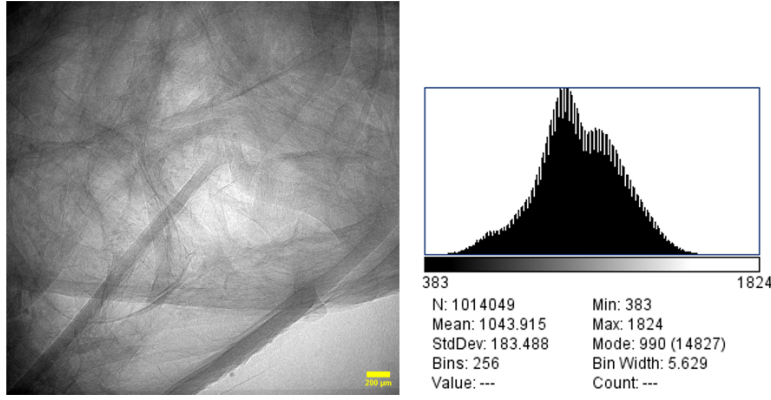
Figure 3.14: Scanned insect (dung-beetle) at SUBIC with the micro-CT scanner. The red arrow indicates where the area of the scan was made.

The sample was scanned with a full angular rotation ranging from  $-93$  to  $93$  degrees, resulting in a total of 1001 projection images. Each projection was exposed to 1 second, with the X-ray source voltage and power set at 60 kV and 5 W, respectively. The acquired projections were binned using a  $2 \times 2$  pixel window, resulting in an image size of  $1007 \times 1007$  pixels and an effective pixel size of  $3.30 \times 3.30 \mu\text{m}^2$ . The sample was positioned 57.207 mm away from the X-ray source and 59.697 mm from the detector resulting in a geometric magnification of 2.04. The optical magnification was  $4\times$ , resulting in a total magnification factor of 8.17. Table 3.3 summarizes the parameters used during the experiment.

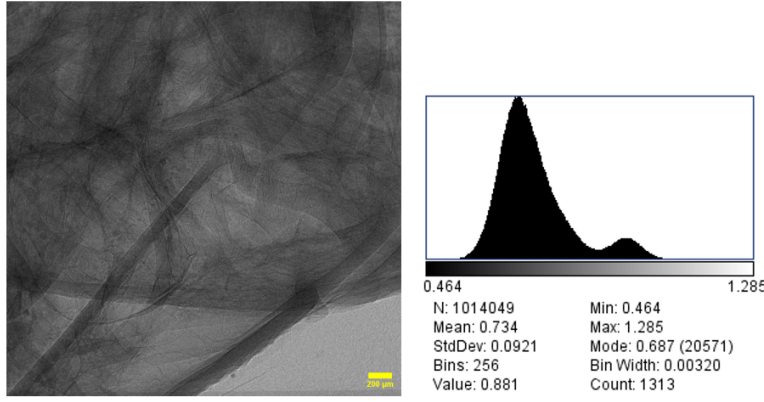
Table 3.3: Insect sample scan parameters.

Parameter	Value
Tube Voltage	60 kV
Power	5 W
Sample Exposure	1 sec
Binning	2x2
Effective Detector Pixel Size	$3.30 \mu\text{m}$
Detector Effective FOV	3.324 mm x 3.324 mm
Pixel Width x Pixel Height	1007 x 1007
Source to Sample Distance	57.207 mm
Sample to Detector Distance	59.697 mm
Objective	4x
Geometric Magnification	2.04
Total Projections	1001
Source Filter	Air

In the theory section, it was mentioned that phase retrieval can also be used as a low-pass filter, and the naming is used interchangeably here. The equation provided in Equation (2.14) is implemented using Python. The steps followed for phase retrieval using the Paganin method are as follows: First, the 1001 projection images collected are flat-field corrected. This correction involves dividing each raw projection image by a reference projection image, a process known as normalization. Figure 3.15 illustrates the 628th phase-contrast projection image along with its corresponding histogram before and after normalization.



(a) Raw projection image of the insect before flat-field correction



(b) Projection image after flat-field correction

Figure 3.15: Projection image before after flat-field correction and corresponding histogram.

Then, by taking the Fourier transform of the projection image in Fig. 3.15b, filtering, and phase retrieval are performed in the frequency domain. The spatial coordinates  $u$  and  $v$  of the filter are calculated using Equation (2.15) and (2.16). The parameters for the filter and retrieval, as shown in Equation (2.17), play a crucial role in determining the performance of the phase retrieval process.

The source-to-detector distance is converted into effective propagation ( $Z_{\text{eff}}$ ) since the employed scanner is a cone-beam system. This conversion is calculated by dividing the source-to-detector distance by the magnification factor ( $M$ ). Another critical consideration is that the scanned insect sample is assumed homogeneous, containing only air and body parts with the same chemical composition. This assumption is a fundamental condition for the Paganin method to work effectively.

Given that the X-ray source used emits polychromatic radiation and is unfiltered (only air), it emits photons at different energy levels. The choice of photon energy is also crucial, as shown in Equation (2.2). Since polychromatic radiation consists of different photon energy levels, the one with a higher photon count level is selected. This choice can be made by manually adjusting the values or by referring to the characteristics' emission lines of the source. Another important factor during the filtering process is the delta-to-beta ratio ( $\delta/\beta$ ) value, this is directly related to the chemical composition of the imaged object and photon energy value since for different photon energy levels, the  $\delta/\beta$  varies.

The overall methodology is illustrated in Fig. 3.16. The projection images and scan metadata are stored in a .txrm file, which is a proprietary format used by the micro-CT scanner. Extraction of the projection and reference images is done through an input/output file handler developed by De Carlo et al.[31]. After normalizing the projection images, the filtering process is performed interactively using a user interface toolbox.

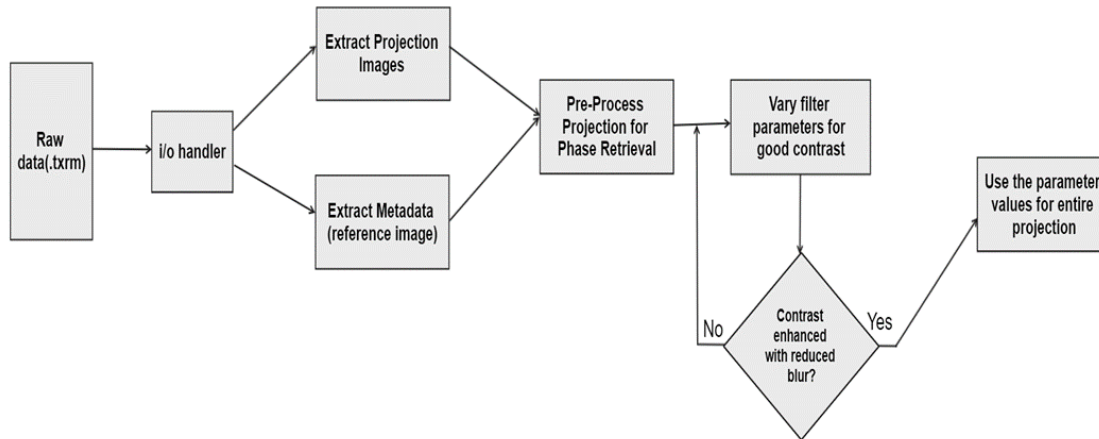


Figure 3.16: The procedure followed for phase retrieval, from data handling to parameter selection.

The proprietary .txrm data format holds the projection images as 2D NumPy arrays and the scan's metadata information in dictionary format. An interface is developed using Python to read this data. After extracting the projection and metadata information, the projection images are pre-processed for phase retrieval. This involves normalizing the projection images based on the incoming X-ray intensity level, which is held as a reference image in a 2-D NumPy matrix. All the projection images are divided by this reference image. A user interface has been developed to simplify the entire process. Users can adjust the relevant parameter values, such as photon energy and delta-beta ratio, to perform the filtering. The programming script has been adapted from [18] and integrated with micro-CT projection data and metadata formats. A portion of the Python code snippet is provided in Appendix B.

## Chapter 4

# Results and Discussion

This chapter covers the results of phase retrieval as a contrast enhancement method for a dung beetle scan and the tomographic reconstruction of helical scanned data compared with conventional scan. With the usage of the Paganin filter, contrast to noise ratio method is used to evaluate the contrast improvement in the tomographic reconstruction.

### 4.1 Helical Scan Reconstruction and Comparison with Conventional Scan

The ability to increase the FOV by moving the detector away from the sample and the detector closer to the sample results in lower overall magnification and resolution. However, by using the helical scan technique, it is possible to increase the FOV of the scanned object without sacrificing resolution and geometric magnification. This makes the further analysis of smaller features easier. By utilizing the FDK reconstruction method, the reconstructed slice of the scanned pencil is shown in Fig. 4.1, both for helical scan and conventional scan, and its respective scanning parameters given in Table 3.1, and Table 3.2. The reconstruction volume is  $501 \times 501 \times 501$  with each voxel size of 0.01 mm for helical and 0.055 mm for conventional. The voxel size is picked according to the effective pixel size of the projection image.

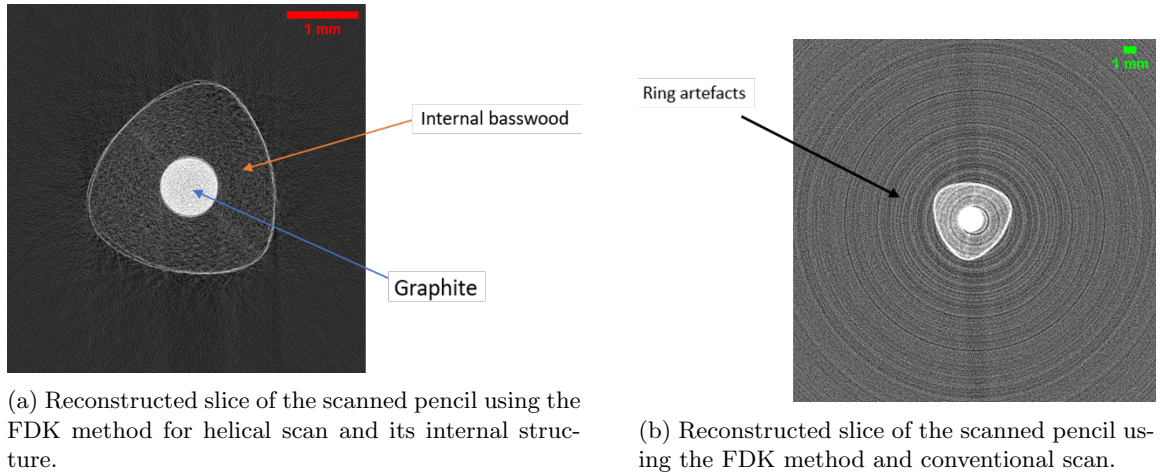


Figure 4.1: Reconstructed slice for both helical and conventional scans.

As the scanned sample is tall and out of the FOV, the helical scan is used to increase FOV by producing a total vertical translational motion of 40 mm with its original FOV of  $18.056 \times 18.056 \text{ mm}^2$  resulting in 58.056 mm FOV vertically. A conventional scan tries to increase the FOV to  $56.736 \times 56.736 \text{ mm}^2$  by moving the source  $-213 \text{ mm}$  away and the detector 49 mm closer to the sample. This leads to a pixelated reconstructed slice with an effective pixel size of  $55.40 \mu\text{m}$  and

reduced geometric magnification, which makes it harder to see small details. The conventional scan reconstruction, shown in Fig. 4.1b, appears more pixelated. This pixelation (grainy appearance) is attributed to the larger voxel size of  $55.45\text{ }\mu\text{m}$ , compared to the helical scan’s voxel size of  $17\text{ }\mu\text{m}$ , and lower geometric magnification, where it is 1.23 for conventional and 3.87 for helical under the same optical magnification ( $0.4\times$ ).

In CT image analysis, the primary objective is to explore the inner composition of a scanned sample, differentiating various materials through visual inspection or image segmentation. Another reconstruction quality to look at is the presence of distortions. The conventional scan is distorted with a ring-shaped artifact in contrast to a helical scan as indicated by the black arrow in Fig. 4.1b. Ring artifacts can be caused by irregular responses by the detector or due to mismatched pixels in the flat-field image during the flat-field correction process or by defective pixels in the detector which gives an irregular response, and during a full circular tomographic reconstruction, it appears as a ring. This ring-like distortion in CT makes it hard to identify objects/fine details. With helical scanning, as the sample is translated vertically, different areas of the detector are covered which limits the possibility of ring artifact as shown in Fig. 4.1a.

The signal-to-noise ratio (SNR) is also another factor we use to measure the CT image quality. The SNR estimation formula is given as follows [8]

$$\text{SNR} = \frac{S}{\sigma}, \quad (4.1)$$

Where  $S$  is the mean signal value of the region of interest (ROI) and  $\sigma$  is its standard deviation. The signal value represents the gray value in the CT image.

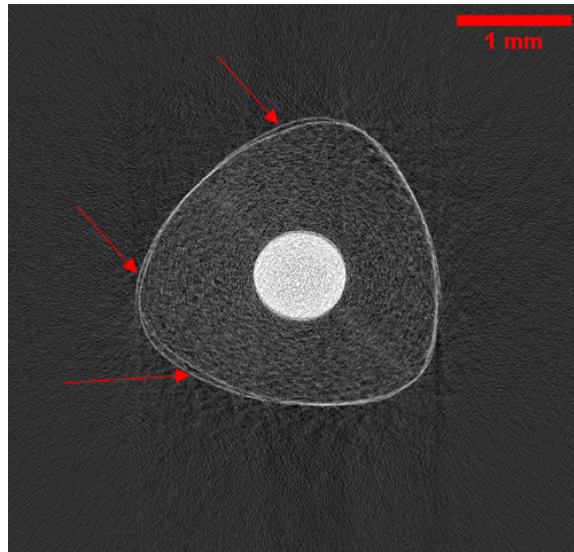
The circular graphite region is taken as the ROI for SNR value comparison since it is the internal structure to be examined, and statistical measurement is taken for both helical and conventional scans with the help of ImageJ software. The values are averaged over the entire volume size i.e. 500 slices. The average value of the signal, standard deviation, and resulting SNR value for the selected ROI are summarized in the table below.

Scan Type	Mean Grayscale for Graphite Region	Standard Deviation	SNR
Helical Scan	0.376	0.078	4.8
Conventional Scan	0.126	0.035	3.6

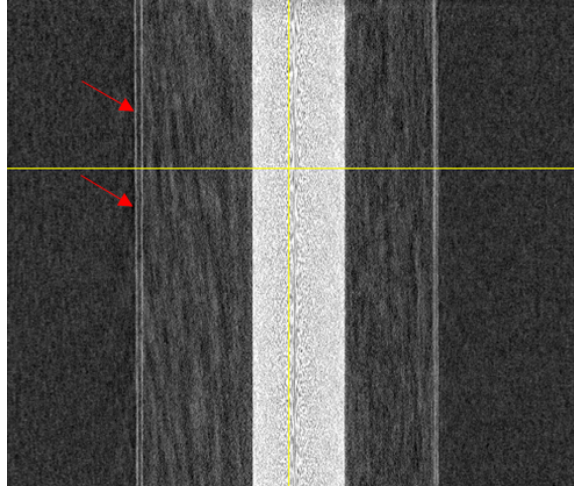
Table 4.1: Comparison of mean grayscale, standard deviation, and SNR for helical and conventional Scans.

As shown in Table 4.1, the ROI (graphite) has a slightly higher SNR for the helical scan at the selected ROI, i.e. graphite region.

Another important factor in helical scanning and using analytical reconstruction FDK is the accurate estimation of the scanning geometry. If they are not selected properly, it can result in motion artifacts where the reconstructed image doesn’t correspond to its physical world appearance. As indicated by the red arrow in Fig. 4.2, the helical scan also suffers from motion artifacts. In this case, the outer reconstruction is not fully complete and solid, unlike the reconstructed slice in Fig. 4.1b. This issue arises from the inaccurate motion compensation during the parametrization of projection images. Since FDK reconstruction is an analytical method, even slight geometric errors can lead to the occurrence of artifacts, such as motion artifacts.



(a) Slice view artifact.



(b) xz plane view of the reconstructed pencil through a helical scan. The red arrow indicates the resulting artifact.

Figure 4.2: Artifacts in the helical scan from a top view and side view.

## 4.2 Phase Retrieval Result and Analysis

With the help of the user interface toolbox developed, the filtering process is done interactively, since it is difficult to constantly vary parameters and save entire projection images to see the results. Figure 4.3 shows a snippet of the user interface designed. The parameters are varied and if blurriness occurs (only low-frequency components are visible) in the projection space, the values need to be reduced/changed and are manually varied until a better contrast/edge enhancement is seen. Then using those parameter values, the phase retrieval is done for the entire 1001 projection images.



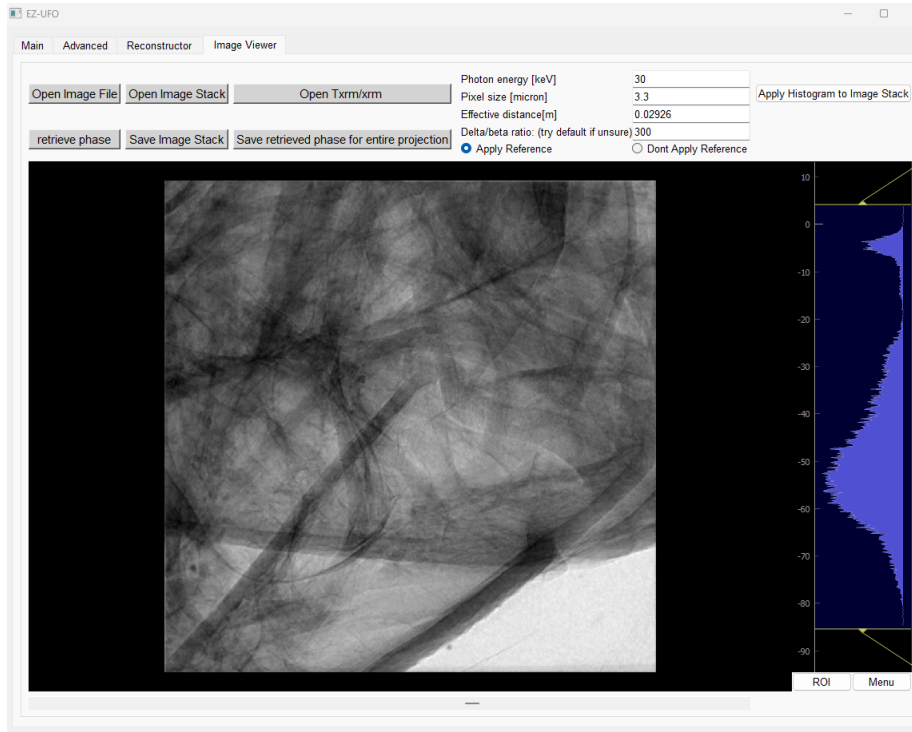


Figure 4.3: A user interface for Paganin phase retrieval. Corresponding parameter values are inserted manually, and the filtering process is done interactively.

To determine the appropriate parameters for phase retrieval, a projection image number that contains more details about the dung beetle is selected. Figure 4.4 displays the 628th projection image, along with its corresponding histogram, after filtering using the Paganin method.

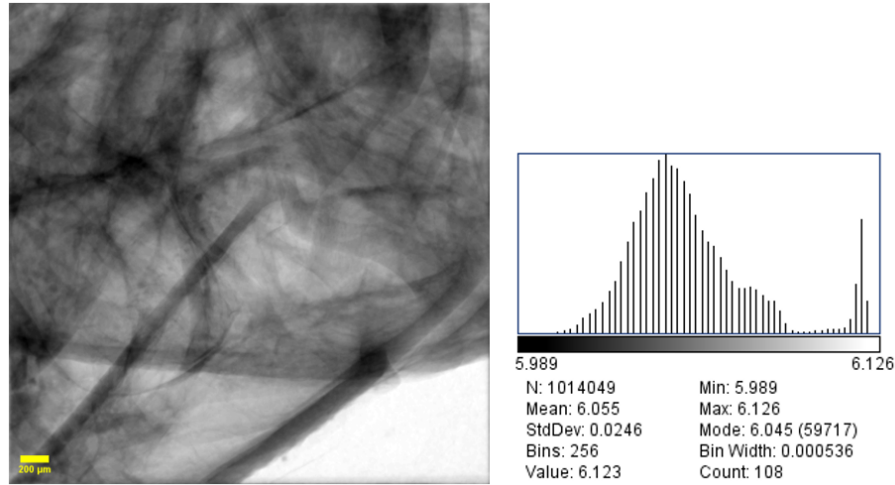


Figure 4.4: Projection image of 3.15b and its histogram after phase retrieval.

Through a straightforward visualization of the histogram and the corresponding projection image, the selected parameters are summarized in Table 4.2 and are subsequently applied to the entire set of projection images. The contrast enhancement effect of the Paganin method becomes more evident and quantifiable after tomographic reconstruction using the micro-CT scanner's reconstruction software. Since the projection alone does not provide much information, it is primarily used for selecting appropriate parameters based on visible contrast and edge enhancement.



Table 4.2: Paganin filter parameter values.

Parameter	Value
Photon Energy	25-30 keV
Effective Pixel Size	3.30 $\mu\text{m}$
Effective Propagation Distance $Z_{\text{eff}}$	29.26 mm
Delta to Beta Ratio ( $\delta/\beta$ )	300

Applying the Paganin phase retrieval as a contrast enhancement for the dung beetle scan results in significant changes in the CT reconstruction result. The reconstructed volume of the scanned sample, both before and after filtering, is shown in Fig. 4.5. A reconstructed slice image, as shown in Fig. 4.5, allows for a direct comparison of the effects before and after phase retrieval. In this image, the black arrow highlights the region of interest i.e., body part, while the yellow arrow indicates the background. The pixel/voxel for each reconstructed slice is  $3.3 \mu\text{m}^2$ .

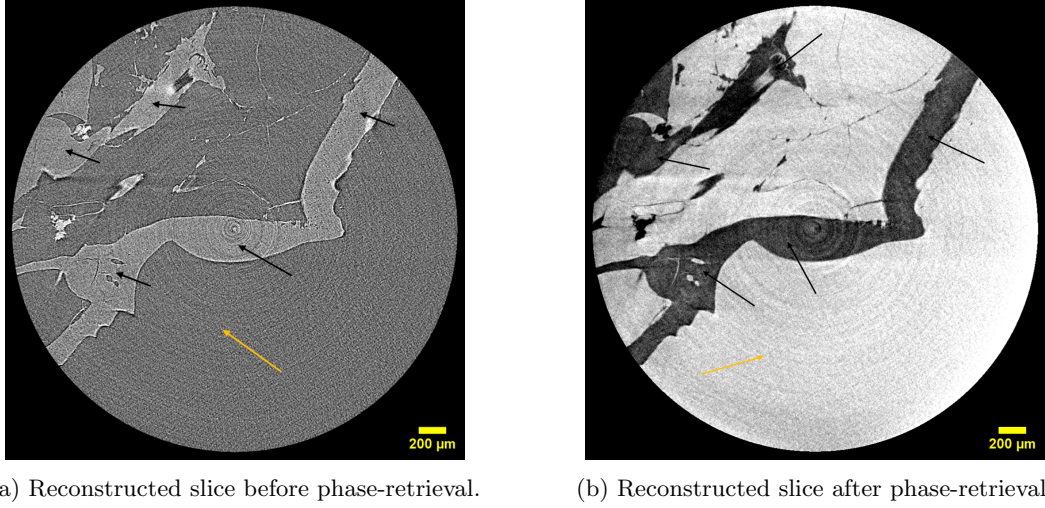


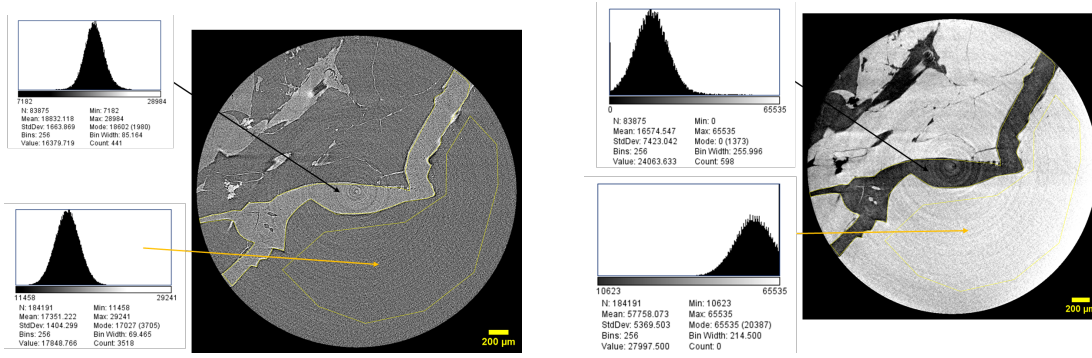
Figure 4.5: Reconstructed slice of dung beetle before and after phase-retrieval.

In order to quantify the contrast value and make a comparison, the contrast-to-noise ratio (CNR) method is used. The contrast-to-noise ratio gives the ratio of the contrast between the signal in a region of interest and the background noise level, and it tells us how well we can see the region of interest (ROI) from the background noise. This ratio is given by the equation below [8]:

$$\text{CNR} = \frac{|\Delta S|}{\sigma}, \quad (4.2)$$

Where  $\Delta S$  is the absolute signal difference (mean value) of the ROI from the background, and  $\sigma$  is the standard deviation of the background. The CNR is calculated by selecting an ROI and comparing it with the background. For the dung beetle projection, it is assumed that there are two ROIs: one representing the background (air) and the other representing the body part of the sample.

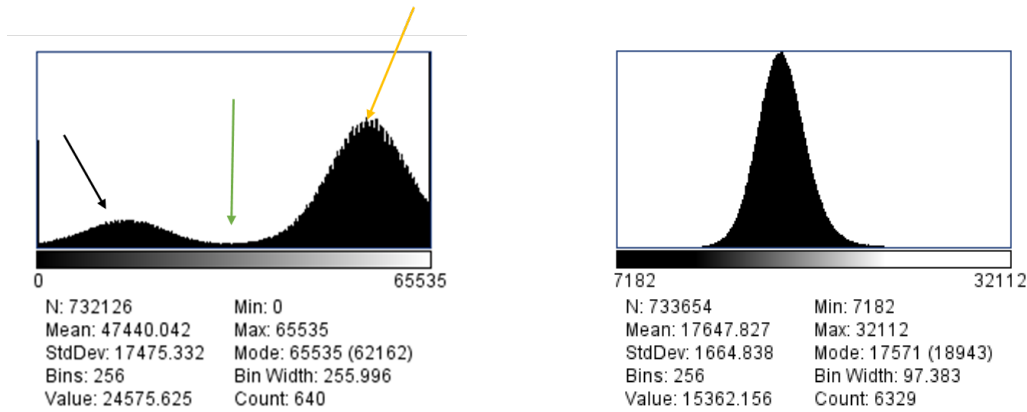
To compare the respective CNR values, two sample slices from the reconstructed image have been used, one before and one after phase retrieval. These slices are selected based on the region where more information (body part) of the imaged sample is found. Figure 4.6 shows the histogram, including the statistical values of the ROI, which is indicated by the black arrow, and the background is indicated by the yellow arrow. The CNR value before for selected ROI in Fig. 4.6a is **0.105**, and after phase retrieval, the selected ROI shown in Fig. 4.6b the CNR value is **7.67**, which is higher than the CNR value in the reconstructed slice before the phase retrieval method. The reconstruction without phase retrieval displays poor contrast, with a noisy background where only edges are distinguishable, while the inner body part is considered as background values (air).



(a) ROI and background with their corresponding histograms before phase-retrieval. (b) ROI and background with their corresponding histograms after phase-retrieval.

Figure 4.6: Reconstructed slice before and after phase-retrieval black arrow indicates the ROI and its corresponding statistical values, while the yellow arrow indicates the background.

After tomographic reconstruction, segmentation is typically carried out to make a quantitative analysis of segmented features. For the segmentation process, it is assumed that there are two distinct phases or ROIs: one representing the body parts of the dung beetle, and the other representing the background. The histogram of the entire slice shown in Fig. 4.6b is depicted in Fig. 4.7a. Through a straightforward visualization of the histogram, it becomes evident how segmentation can be done. The presence of two distinct peaks in the histogram shown in Fig. 4.7a provides clear indicators. The higher peak, highlighted by the yellow arrow, represents the distribution for the background, while the peak denoted by the black arrow represents the distribution for the body part of the imaged sample, which serves as the ROI. By simply selecting an appropriate threshold value indicated by the green arrow, segmentation can be performed and the resulting volumetric image, rendered in 3D, will be well-suited for subsequent quantitative analysis.

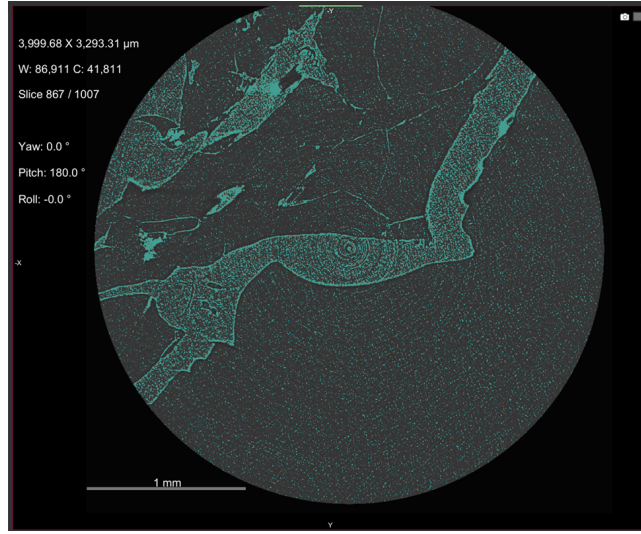


(a) Histogram for the whole slice in figure 4.6b. (b) Histogram for the whole slice for figure 4.6a.

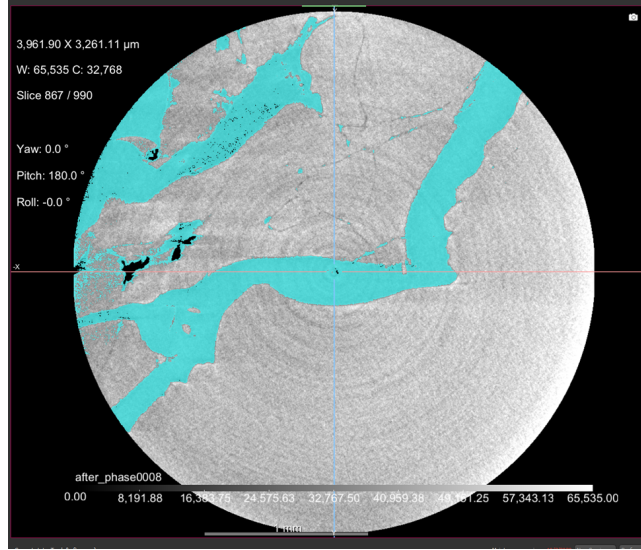
Figure 4.7: Corresponding histograms for the entire slice in Fig. 4.6.

When looking at the histogram of Fig. 4.7b, only one peak is present, this makes segmenting the ROI from the background difficult. This was also further indicated by its lower contrast-to-noise ratio value.

Segmentation and 3-D rendering of the entire reconstructed image slice were performed using Dragonfly software. Dragonfly facilitates further qualitative analysis, including dimensional assessments through 3-D rendering of reconstructed CT slices. Figure 4.8 illustrates the same segmentation performed on the reconstructed slices using the threshold method, in order to distinguish a distinct region between the background and the body of the scanned sample.



(a) Segmented slice before phase-retrieval.



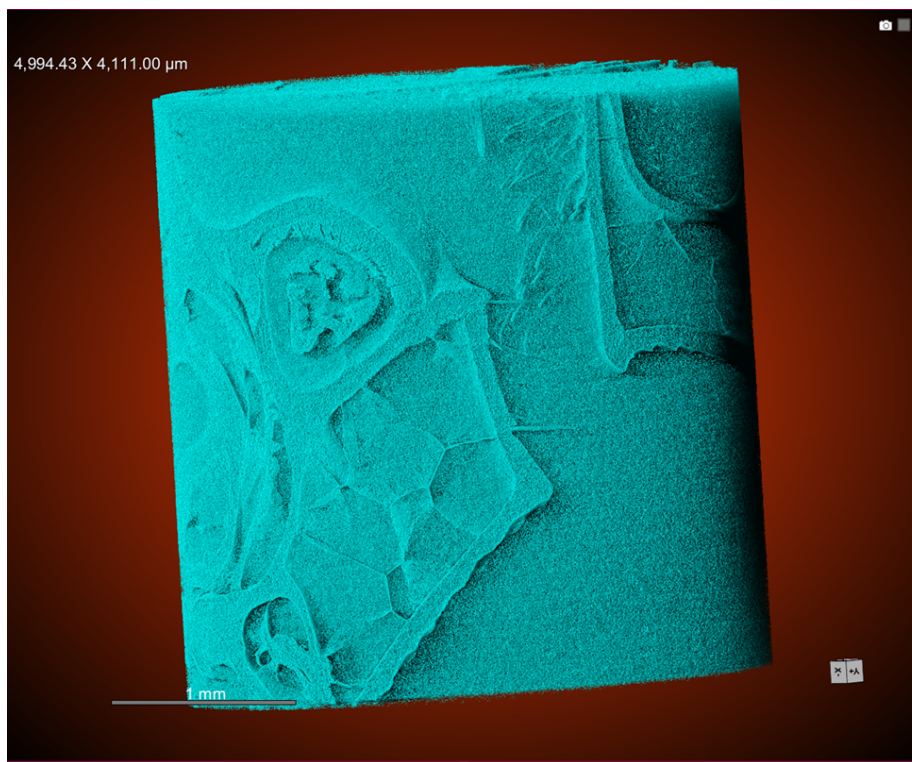
(b) Segmented slice after phase-retrieval.

Figure 4.8: Segmentation of ROI using thresholding method before and after phase retrieval. The orange coloring is the background and black is the ROI.

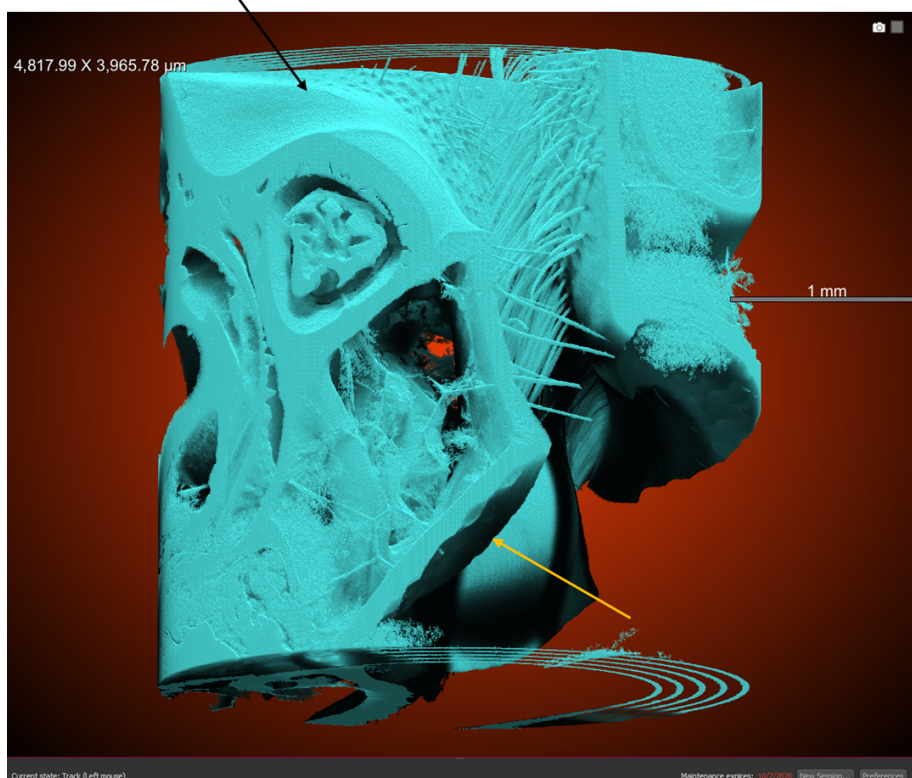
It can be seen that the segmented image in Fig. 4.8a without phase retrieval includes the background image as part of the body sample, as indicated by the blue dots on the background complicating the segmentation task. However, for segmentation done after phase retrieval as indicated in Fig. 4.8b, the background is segmented separately from the ROI, as indicated by the separated coloring.

After doing segmentation with the help of Dragonfly, the rendered 3-D image of the segmented part/ROI of the sample before and after phase retrieval is shown in Fig. 4.9. Through visualization, it is harder to make further quantitative analysis for the rendered image before image retrieval as the image is filled with background incorrectly represented as the body part of the sample i.e. most of the area of ROI is segmented as background. Whereas in the case of Fig. 4.9b, it clearly shows stronger edge enhancement and small features of the sample two eyes of the sample, i.e. upper-left eye and lower left eye can be seen. This is due to the larger value in CNR compared to the reconstructed image before phase retrieval.





(a) Rendered 3-D of dung beetle before phase-retrieval



(b) Rendered 3-D of dung beetle after phase-retrieval. The black arrow indicates the upper-left eye and the yellow arrow is the lower-left eye. See Appendix A for a better angle view.

Figure 4.9: 3-D rendered image of the scanned sample before and after phase-retrieval

## Chapter 5

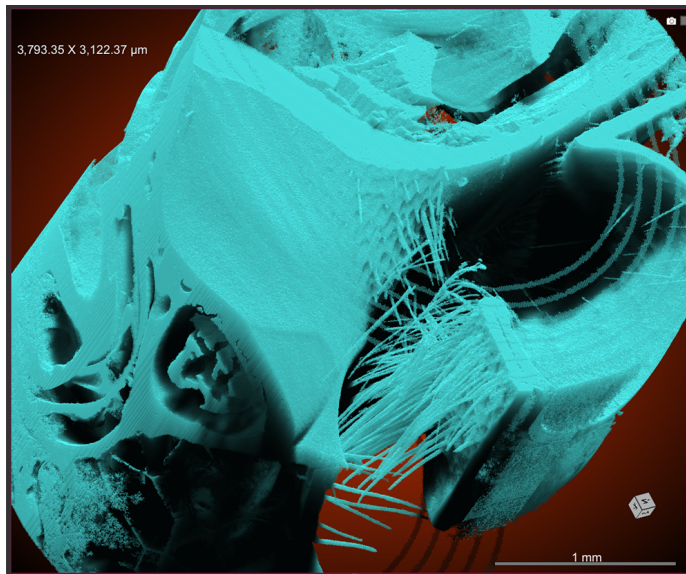
# Conclusion and Future Work

The Paganin phase retrieval method has proven to be successful in enhancing the contrast in the images of weakly attenuating samples, imaged with the phase contrast method using hard X-rays. This method has significantly improved contrast levels, making segmentation and 3-D rendering more straightforward. In a selected region of interest (ROI), the computed contrast-to-noise ratio (CNR) exhibited an increase from 0.105 to 7.67. Having demonstrated the efficiency of phase retrieval, my user-friendly software for reading the CT scan in a TXRM format and interactively choosing appropriate parameters for phase retrieval can be an essential asset for researchers in the whole world, especially the labs where the Xradia micro-CT system is used. The special data format has made post-processing very challenging for researchers who are not familiar with image processing or programming. With the developed software, the phase retrieval process becomes straightforward and easy to evaluate.

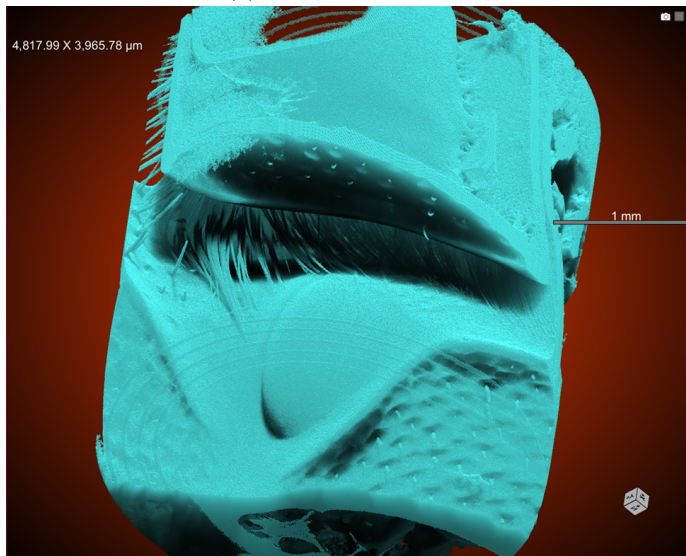
Furthermore, the development of a helical scanning technique has expanded the field of view (FOV) along the vertical axis. This technique effectively utilizes the Feldkamp-Davis-Kress (FDK) algorithm, implemented through the open-source tomographic image processing toolbox ASTRA. It achieves this by parametrizing the circular cone-beam geometry and integrating scanning with a commercial micro-CT scanner. The helical scanning technique is especially valuable for scanning elongated samples larger than the FOV, exhibiting uniform properties along their length. Importantly, it achieves this without sacrificing resolution and magnification during the scan. It eliminates the need for extensive adjustments to the source-sample-detector geometry to fit the scanned sample into the FOV, thereby achieving optimal resolution and magnification through vertical translational motion. Others may consider conducting quantitative analyses on the reconstructed helical data for future work. This could involve tasks such as 3D rendering and dimensional measurements. Additionally, investigating the integration of iterative reconstruction algorithms to enhance reconstruction quality is a potential avenue for improvement. Furthermore, exploring diverse sample shapes and properties will contribute to the validation and broadening of the applicability of these techniques.

## Appendix A

### Additional figures



(a) Upper left eye view



(b) Lower left eye view

Figure A.1: 3-D rendered image of the scanned sample upper and lower left eye part.

## Appendix B

# Snippet of Python Code for Paganin Phase Retrieval

Listing B.1: Python Code [18]

```
1 import numpy as np
2 from paganin_method.utilities import resize
3
4 class TIEHOM:
5     """
6
7     Transport of Intensity Equation for homogeneous objects(TIEHOM)
8     Paganin Phase Retrieval Method
9     """
10
11     """Base class for 2D phase retrieval algorithms.
12
13     Parameters
14     -----
15     Projection Image
16     shape: Size of images (ny, nx) for creation of frequency variables
17           etc.
18     pixel_size: float effective pixel size in m.
19     Distance: list of floats, optional Effective propagation distances
20              in m.
21     Energy: float, optional Effective energy in keV.
22     delta_beta: float, Material dependent ratio delta over beta.
23
24     Attributes
25     -----
26     nx: int Number of pixels in the horizontal direction.
27     ny : int Number of pixels in the horizontal direction.
28     energy: float Energy in keV.
29     distance: NumPy array Effective propagation distances in m.
30     sample_frequency: float Reciprocal of pixel size in length.
31     nfx: int Number of samples in Fourier domain (horizontal).
32     nfy: int The number of samples in the Fourier domain (vertical).
33     fx: NumPy array Frequency variable (horizontal), calculated by
34         frequency_variable.
35     fy: NumPy array Frequency variable (vertical).
36     """
37
38     def __init__(self, delta_beta=500, **kwargs):
39         self.lengthscale = 10e-6
40         self._delta_beta = delta_beta
41         self.padding = 2
```

```

39     self.lengthscale = 10e-6 #
40     self.nx = kwargs["shape"][1] #Number of pixels along the column
41     self.ny = kwargs["shape"][0] #Number of pixels along the row
42     self.pixel_size = kwargs["pixel_size"] #pixel size in m
43     self.distance = np.array(kwargs["distance"]) #Effective propagation
        distance in m
44     self.energy = kwargs["energy"] #Photon energy
45
46     self.nfx = self.padding * self.nx
47     self.nfy = self.padding * self.ny
48
49     if 'pad' in kwargs:
50         self.padding = kwargs['pad']
51
52     if (type(self.pixel_size) == float) or (
53         type(self.pixel_size) == np.float64): # If x,y pixelsizes
        are not given, assign them
54         self.pixel_size = np.array([self.pixel_size, self.pixel_size])
55     elif type(self.pixel_size) == list:
56         self.pixel_size = np.array(self.pixel_size)
57     self.sample_frequency = self.lengthscale / self.pixel_size #
        sampling frequency
58     self.fx, self.fy = self.frequency_variable(self.nfx, self.nfy, self.
        sample_frequency)
59
60
61 @property
62 def delta_beta(self):
63     """Material dependent ratio delta over beta (float)."""
64     return self._delta_beta
65
66 @delta_beta.setter
67 def delta_beta(self, delta_beta):
68     """ Recalculates dependent factors on setting (float)."""
69     if delta_beta != self._delta_beta:
70         self._delta_beta = delta_beta
71         self._compute_factors()
72 def frequency_variable(self, nfx, nfy, sample_frequency):
73     """
74     Calculate the spatial frequency variables.
75
76     Parameters
77     -----
78     nfx : int
79         Number of samples in x direction
80     nfy : int
81         Number of samples in y direction
82     sample_frequency : float
83         Reciprocal of pixel size in 1/m
84
85     Returns
86     -----
87     nparray
88         Frequency variables as an array of size [nfy, nfx, 2]
89
90     """
91
92     if type(sample_frequency) == int:
93         sample_frequency = np.array([sample_frequency, sample_frequency
94             ]) # TODO: refactor
95
96     x = 0

```



```

96     x = np.append(x, np.linspace(sample_frequency[0] / nfx,
97                                 sample_frequency[0] / 2, nfx // 2))
97     x = np.append(x, np.linspace(-sample_frequency[0] / 2 +
98                                 sample_frequency[0] / nfx,
99                                 int(nfx // 2 - 1 + (np.ceil(nfx / 2) -
100                                     nfx // 2))))
100
101     y = 0
101     y = np.append(y, np.linspace(sample_frequency[1] / nfy,
102                                 sample_frequency[1] / 2, nfy // 2))
102     y = np.append(y, np.linspace(-sample_frequency[1] / 2 +
103                                 sample_frequency[1] / nfy, -sample_frequency[1] / nfy,
104                                 int(nfy // 2 - 1 + (np.ceil(nfy / 2) -
105                                     nfy // 2))))
104
105     return np.meshgrid(x, y)
105
106 #computing factors for the Paganin method
107 def _compute_factors(self):
108     """ Calculates Transport factors of Intensity Equation for
109         homogeneous object """
109
110
111     """ Wavelength based on energy (float)"""
112     self.Lambda=12.4e-10 / self.energy
113     """Fresnel number calculated from energy and distance (float)"""
114     self.Fresnel_number=self.Lambda * self.distance / (self.lengthscale
115                                                         ** 2) #Fresnel Number for near-field regime of Phase-Contrast
116                                                         imaging
115     self.TIEHOM_factor = 1 + self.Fresnel_number * np.pi * self.
116         delta_beta * ((self.fx ** 2) + (self.fy ** 2))
116
117 def _algorithm(self, image, positions=None):
118     " Phase Reconstruction"
119     FID = np.fft.fft2(image) #2D Fast Fourier Transform of the
120         porjection image
120
121     #Retrieve the Phase and attenuation
122     phase = 1 / 2 * self.delta_beta * np.log(np.real(np.fft.ifft2(FID[
123         positions[0]] / self.TIEHOM_factor[positions[0]])))
123     attenuation = -1 / (self.delta_beta) * phase
124
125     return phase, attenuation

```

## Appendix C

# Helical Scan Data Acquisition API with Python

Listing C.1: Python Code

```
1 import os, sys
2 from XradiaPy.Core import XRM as API
3 from XradiaPy.Recipe import Recipe
4 import time
5 import numpy as npy
6
7 def helical_motion(pt, np):
8
9     '''
10     # parameters
11     pt= total vertical pitch in micrometer
12     np=number of projections per 360-degree
13     # Attributes
14     ystep= sample's pitch along the Y-axis per projection in micrometer
15     angle_mvm=sample's angular movement per projection in degrees
16     '''
17     times_array = npy.zeros((np, 1))
18     ystep=-1.0*(pt/(np - 1.0)) #pitch amount for every projection
19     folder = "D:\Data\Yoseph\last_scan_for_helical\last_scan_for_helical" #
20     Directory path to save projection Images
21     angle_mvm = 360.0 / (np - 1.0) #angle movement for every projection
22     theta_pos=API.GetAxisPosition("Sample theta") #
23     y_pos = API.GetAxisPosition("Sample Y")
24     if theta_pos != 180 and y_pos !=8654.5: #if sample holder angular and Y-
25     axis position is not at the desired coordinates, move it
26         API.MoveAxisAbsolute("Sample Theta", -180.0, True) # home position
27         API.MoveAxisAbsolute("Sample Y", -8654.5, True) #Micrometer
28
29     API.MoveAxisAbsolute("Source Z", -53.53, True)#Source Z-axis original
30     position mm
31     API.MoveAxisAbsolute("Detector Z", 153.380, True)# Detector Z-axis
32     original position mm
33     API.TurnXrayOn(80.0, 7.0) #Turn X-ray on Specified voltage kV and power
34     W
35     API.SetObjective("0.4X") #Set optical magnification to 0.4X
36     for i in range(0, np):
37         sampleTheta = API.GetAxisPosition("Sample theta") #Store angular
38         position value
39         sampleY = API.GetAxisPosition("Sample Y") #store sample Y-axis
40         position value
41         filename = folder + "SingleAcq" + "Proj" + str(int(i)) + "Y_pst" +
```

```

        str(int(sampleY)) + ".xrm"
35     start_time_method1 = time.time()
36     ret_val = API.SingleAcquisition(1, 2, filename) #take acquisition
        image with specified exposure time (1sec) and binning size 2x2
37     end_time_method1 = time.time()
38     time_method1 = (end_time_method1 - start_time_method1) * 1e6 #in
        microseconds
39     times_array[i] = [time_method1]
40     if ret_val==True: #check if the previous acquisition was successful
        and proceed to angular and vertical translation movement
41         API.MoveAxisRelative("Sample Theta", angle_mvm, True)
42         API.MoveAxisRelative("Sample Y", ystep, True)
43     else:
44         print "Didnt take acquisition image"
45         print "angle =", sampleTheta
46     return times_array
47
48
49 # Press the green button in the gutter to run the script.
50 if __name__ == '__main__':
51     data = helical_motion(pt=20000, np=800)

```

## Appendix D

# Helical Scan Geometry Parametrization and Tomographic Reconstruction in ASTRA using Python

Listing D.1: Python Code

```
1 import numpy as np
2 import astra
3 import os
4 import imageio
5 import xrmreader
6 projection_data = "C:\\Users\\SUBIC\\PycharmProjects\\astra-toolbox\\
    helical_scan_python\\pencil_total_new.txrm" # reading helical
    projection metadata
7 metadata = xrmreader.read_metadata(projection_data)
8 my_angle = metadata['thetas']
9 #number of voxels per mm in one direction (higher = larger res)
10 voxel_per_mm = 10
11 #Data path where the pre-processed images are stored
12 data_path = 'C:\\Users\\SUBIC\\PycharmProjects\\astra-toolbox\\
    helical_scan_python\\pencil_for_reco' # helical data path
13 #recon_path to store reconstructed slices
14 recon_path = 'C:\\Users\\SUBIC\\PycharmProjects\\astra-toolbox\\
    helical_scan_python\\actual_recon_pen'
15 ### Load pre-processed projection data
16 data_path_full = os.path.join(data_path)
17 projs_name = 'fdk_pos2_ass1_vmm1_{:06}.tiff'
18 #Number of pixels along the row and column
19 projs_rows = 1024
20 projs_cols = 1024
21 n_pro = metadata['number_of_images'] #number of projection images
22 # projection file indices, we need to read the projection in reverse order
    due to the portrait mode acquisition
23 projs_idx = range(n_pro-1, -1, -1)
24 vectors = np.zeros((n_pro, 12)) #creating empty nx12 vector to hold scanning
    geometry specification
25 # Create the numpy array which will receive projection data from tiff files
26 projs = np.zeros((n_pro, projs_rows, projs_cols), dtype=np.float32)
27 for i in range(n_pro):
28     projs[i] = imageio.imread(os.path.join(data_path_full, projs_name.format
        (projs_idx[i])))
29 array_length = 800
```

```

30 increment = 1 # 1
31 my_array = np.arange(0, array_length * increment, increment)
32 ### pre-process data
    #####
33 print('pre-process data', flush=True)
34 #Change the position of the projection image numpy array to ASTRA format
35 projs = np.transpose(projs, (1, 0, 2))
36 projs = np.ascontiguousarray(projs)
37 ### FDK reconstruction #
38 # size of the reconstruction volume in voxels
39 vol_sz = 3 * (50 * voxel_per_mm + 1,) #vol_sz = (1800,501,501)
40 # size of a cubic voxel in mm
41 vox_sz = 0.01
42 # empty numpy array holding the reconstruction volume
43 vol_rec = np.zeros(vol_sz, dtype=np.float32)
44 #Scaling the Volume geometry along the XYZ, to the voxel size since ASTRA by
    default assumes it is 1
45 vol_geom = astra.create_vol_geom(vol_sz)
46 vol_geom['option']['WindowMinX'] = vol_geom['option']['WindowMinX'] * vox_sz
47 vol_geom['option']['WindowMaxX'] = vol_geom['option']['WindowMaxX'] * vox_sz
48 vol_geom['option']['WindowMinY'] = vol_geom['option']['WindowMinY'] * vox_sz
49 vol_geom['option']['WindowMaxY'] = vol_geom['option']['WindowMaxY'] * vox_sz
50 vol_geom['option']['WindowMinZ'] = vol_geom['option']['WindowMinZ'] * vox_sz
51 vol_geom['option']['WindowMaxZ'] = vol_geom['option']['WindowMaxZ'] * vox_sz
52 recon_path_full = os.path.join(recon_path)
53 eff_pxs = 0.02 #effective pixel size in mm
54 pevp = 0.05 # pitch amount per-projection in mm
55 #creating a nx12 vector to hold projection vector specifications for every
    angular and vertical translation motion
56 for i in range(len(my_angle)):
57     #HELEICAL SCAN GEOMETRY
58     vectors[i, 0] = np.sin(my_angle[i]) * 53.3
59     vectors[i, 1] = -np.cos(my_angle[i]) * 53.3
60     vectors[i, 2] = pevp*eff_pxs*my_array[i] #-pevp*eff_pxs*my_array[
        i] # Either up or down depends on the polarity
61     # center of the detector
62     vectors[i, 3] = -np.sin(my_angle[i]) * 153.38
63     vectors[i, 4] = np.cos(my_angle[i]) * 153.38
64     vectors[i, 5] = pevp*eff_pxs*my_array[i] #-pevp*eff_pxs*my_array[i
        ]
65     # vector from detector pixel (0,0) to (0,1)
66     vectors[i, 6] = np.cos(my_angle[i]) * eff_pxs
67     vectors[i, 7] = np.sin(my_angle[i]) * eff_pxs
68     vectors[i, 8] = 0
69     # vector from detector pixel (0,0) to (1,0)
70     vectors[i, 9] = 0
71     vectors[i, 10] = 0
72     vectors[i, 11] = eff_pxs
73 #Specifying projection and Volume geometry space to ASTRA
74 proj_geom = astra.create_proj_geom('cone_vec', projs_rows, projs_cols,
    vectors)
75 vol_id = astra.data3d.link('-vol', vol_geom, vol_rec)
76 proj_id = astra.data3d.link('-sino', proj_geom, projs)
77 #Creating ASTRA configuration that sets up reconstruction algorithm,
    projection and volume geometry
78 cfg_fdk = astra.astra_dict('FDK_CUDA') #SIRT3D_CUDA
79 cfg_fdk['ProjectionDataId'] = proj_id
80 cfg_fdk['ReconstructionDataId'] = vol_id
81 cfg_fdk['option'] = {}
82 cfg_fdk['option']['ShortScan'] = False
83 alg_id = astra.algorithm.create(cfg_fdk)
84 # running FDK algorithm

```

```
85 astra.algorithm.run(alg_id)
86 # release memory allocated by ASTRA structures
87 astra.algorithm.delete(alg_id)
88 astra.data3d.delete(proj_id)
89 astra.data3d.delete(vol_id)
90 ### Saving Reconstruction Result as a separate tiff file ###
91 for i in range(vol_sz[0]):
92     slice_path = os.path.join(recon_path_full, 'helical_{:06}.tiff'.format(
93         i))
94     imageio.imwrite(slice_path, vol_rec[i,...])
```

# Bibliography

- [1] L. D. Chiffre, S. Carmignato, J.-P. Kruth, R. Schmitt, and A. Weckenmann, “Industrial applications of computed tomography,” *CIRP Annals*, vol. 63, no. 2, pp. 655–677, 2014. [Online]. Available: <https://doi.org/10.1016/j.cirp.2014.05.011>
- [2] M. Krumm, C. Sauerwein, V. Hämmerle, and S. Heile, “Robotic x-ray computed tomography system for fast automated non-destructive testing of joints in large assemblies and its application in automotive production,” in *12th European Conference on Non-Destructive Testing (ECNDT 2018)*. Gothenburg: Bruker Belgium NV, June 2018.
- [3] D. Paganin, S. C. Mayo, T. E. Gureyev, P. R. Miller, and S. W. Wilkins, “Simultaneous phase and amplitude extraction from a single defocused image of a homogeneous object,” *Journal of Microscopy*, vol. 206, no. 1, pp. 33–40, Apr. 2002. [Online]. Available: <https://doi.org/10.1046/j.1365-2818.2002.01010.x>
- [4] W. van Aarle, W. J. Palenstijn, J. Cant, E. Janssens, F. Bleichrodt, A. Dabrovolski, J. D. Beenhouwer, K. J. Batenburg, and J. Sijbers, “Fast and flexible x-ray tomography using the astra toolbox,” *Opt. Express*, vol. 24, no. 22, pp. 25 129–25 147, Oct 2016. [Online]. Available: <https://opg.optica.org/oe/abstract.cfm?URI=oe-24-22-25129>
- [5] H. Miao, H. Juan Zhao, F. Gao, and S. run Gong, “Implementation of FDK reconstruction algorithm in cone-beam CT based on the 3d shepp-logan model,” in *2009 2nd International Conference on Biomedical Engineering and Informatics*. IEEE, 2009. [Online]. Available: <https://doi.org/10.1109/bmei.2009.5304987>
- [6] A. Maier, S. Steidl, V. Christlein, and J. Hornegger, Eds., *Medical Imaging Systems*. Springer International Publishing, 2018. [Online]. Available: <https://doi.org/10.1007/978-3-319-96520-8>
- [7] U. Lundström, “Phase-contrast x-ray carbon dioxide angiography,” Ph.D. dissertation, KTH, Biomedical and X-ray Physics, 2014, qC 20140113.
- [8] T. Zhou, “Laboratory x-ray phase-contrast imaging : Methods and comparisons,” Ph.D. dissertation, KTH, Biomedical and X-ray Physics, 2016, qC 20160921.
- [9] A. Maier, S. Steidl, V. Christlein, and J. Hornegger, Eds., *Medical Imaging Systems*. Springer International Publishing, 2018. [Online]. Available: <https://doi.org/10.1007/978-3-319-96520-8>
- [10] S. Reza, “Advanced x-ray detectors for industrial and environmental applications,” Ph.D. dissertation, Mid Sweden University, Department of Electronics Design, 2016.
- [11] X. Ou, X. Chen, X. Xu, L. Xie, X. Chen, Z. Hong, H. Bai, X. Liu, Q. Chen, L. Li, and H. Yang, “Recent development in x-ray imaging technology: Future and challenges,” *Research*, vol. 2021, 2021. [Online]. Available: <https://spj.science.org/doi/abs/10.34133/2021/9892152>
- [12] C. Zuo, J. Li, J. Sun, Y. Fan, J. Zhang, L. Lu, R. Zhang, B. Wang, L. Huang, and Q. Chen, “Transport of intensity equation: a tutorial,” *Optics and Lasers in Engineering*, vol. 135, p. 106187, Dec. 2020. [Online]. Available: <https://doi.org/10.1016/j.optlaseng.2020.106187>
- [13] S. Reza, “Phase-contrast and spectroscopic x-ray imaging for paperboard quality assurance,” 2014.

- [14] A. Burvall, U. Lundström, P. A. C. Takman, D. H. Larsson, and H. M. Hertz, “Phase retrieval in x-ray phase-contrast imaging suitable for tomography,” *Opt. Express*, vol. 19, no. 11, pp. 10 359–10 376, May 2011. [Online]. Available: <https://opg.optica.org/oe/abstract.cfm?URI=oe-19-11-10359>
- [15] T. Weitkamp, D. Haas, D. Wegrzynek, and A. Rack, “iANKAphase/i: software for single-distance phase retrieval from inline x-ray phase-contrast radiographs. erratum,” *Journal of Synchrotron Radiation*, vol. 20, no. 1, pp. 205–205, Dec. 2012. [Online]. Available: <https://doi.org/10.1107/s0909049512044871>
- [16] T. Faragó, S. Gasilov, I. Emslie, M. Zuber, L. Helfen, M. Vogelgesang, and T. Baumbach, “Tofu: a fast, versatile and user-friendly image processing toolkit for computed tomography,” *Journal of Synchrotron Radiation*, vol. 29, no. 3, pp. 916–927, May 2022. [Online]. Available: <https://doi.org/10.1107/S160057752200282X>
- [17] N. T. Vo, R. C. Atwood, M. Drakopoulos, and T. Connolley, “Data processing methods and data acquisition for samples larger than the field of view in parallel-beam tomography,” *Opt. Express*, vol. 29, no. 12, pp. 17 849–17 874, Jun 2021. [Online]. Available: <https://opg.optica.org/oe/abstract.cfm?URI=oe-29-12-17849>
- [18] M. Langer, Y. Zhang, D. Figueirinhas, J.-B. Forien, K. Mom, C. Mouton, R. Mokso, and P. Villanueva-Perez, “PyPhase – a Python package for X-ray phase imaging,” *Journal of Synchrotron Radiation*, vol. 28, no. 4, pp. 1261–1266, Jul 2021. [Online]. Available: <https://doi.org/10.1107/S1600577521004951>
- [19] I. Häggmark, “Phase-contrast x-ray imaging of complex objects,” Ph.D. dissertation, KTH, Biomedical and X-ray Physics, 2021.
- [20] Algotom, “Section 1.3: Basic components of an x-ray tomography system,” Algotom documentation, 2021, retrieved August 4, 2023. [Online]. Available: <https://algotom.readthedocs.io/en/latest/toc/section1/section1.3.html>
- [21] J. Sunnegårdh, “Iterative filtered backprojection methods for helical cone-beam ct,” Ph.D. dissertation, Linköping UniversityLinköping University, Computer Vision, The Institute of Technology, 2009.
- [22] M. Soleimani and T. Pengpen, “Introduction: A brief overview of iterative algorithms in x-ray computed tomography,” *Philosophical transactions. Series A, Mathematical, physical, and engineering sciences*, vol. 373, 06 2015.
- [23] J. Radon, “On the determination of functions from their integral values along certain manifolds,” *IEEE Transactions on Medical Imaging*, vol. 5, no. 4, pp. 170–176, Dec. 1986. [Online]. Available: <https://doi.org/10.1109/tmi.1986.4307775>
- [24] A. Maier, S. Steidl, V. Christlein, and J. Hornegger, Eds., *Medical Imaging Systems*. Springer International Publishing, 2018. [Online]. Available: <https://doi.org/10.1007/978-3-319-96520-8>
- [25] —, *Medical Imaging Systems*. Springer International Publishing, 2018. [Online]. Available: <https://doi.org/10.1007/978-3-319-96520-8>
- [26] A. Biguri, M. Dosanjh, S. Hancock, and M. Soleimani, “Tigre: a matlab-gpu toolbox for cbct image reconstruction,” *Biomedical Physics Engineering Express*, vol. 2, no. 5, p. 055010, sep 2016. [Online]. Available: <https://dx.doi.org/10.1088/2057-1976/2/5/055010>
- [27] L. A. Feldkamp, L. C. Davis, and J. W. Kress, “Practical cone-beam algorithm,” *Journal of the Optical Society of America A*, vol. 1, no. 6, p. 612, Jun. 1984. [Online]. Available: <https://doi.org/10.1364/josaa.1.000612>
- [28] G. L. Zeng, *Basic Principles of Tomography*. Berlin, Heidelberg: Springer Berlin Heidelberg, 2010, pp. 95–96. [Online]. Available: [https://doi.org/10.1007/978-3-642-05368-9\\_1](https://doi.org/10.1007/978-3-642-05368-9_1)



- [29] L. Li, Y. Xing, Z. Chen, L. Zhang, and K. Kang, “A new curve-filtered FDK-type algorithm for circular cone-beam CT reconstruction,” in *IEEE Nuclear Science Symposium & Medical Imaging Conference*. IEEE, Oct. 2010. [Online]. Available: <https://doi.org/10.1109/nssmic.2010.5874182>
- [30] *ZEISS Xradia Versa User’s Guide*, Carl Zeiss X-ray Microscopy, Inc., January 2021, © 2014 – 2021 Carl Zeiss X-ray Microscopy, Inc. All Rights Reserved.
- [31] F. De Carlo, D. Gursoy, F. Marone, M. Rivers, D. Y. Parkinson, F. Khan, N. Schwarz, D. J. Vine, S. Vogt, S. C. Gleber, S. Narayanan, M. Newville, A. Lanzirotti, Y. Sun, Y. P. Hong, and C. Jacobsen, “Scientific data exchange: A schema for hdf5-based storage of raw and analyzed data,” *Journal of Synchrotron Radiation*, vol. 21, no. 6, pp. 1224–1230, 2014.